Materials & Design 268 (2026) 116599

Contents lists available at ScienceDirect

Materials & Design

journal homepage: www.elsevier.com/locate/matdes

Bimetallic Al–Fe composites with tailored properties produced by cold spray additive manufacturing☆

Kiran Tulasagiri Raddi, Asghar Heydari Astaraee, Sara Bagherifard *

Department of Mechanical Engineering, Politecnico di Milano, 20156 Milan, Italy

ARTICLE INFO

Keywords:
Solid-state deposition
Multi-material
Metal-matrix composite
Metal-particle reinforcement

ABSTRACT

Cold spray enables multi-material additive manufacturing through solid-state bonding, thereby reducing intermetallic formation and thermal residual stresses typical of fusion-based manufacturing routes. This study establishes a composition–structure–property framework for cold sprayed Al–Fe bimetallic composites produced by online powder mixing by varying Fe content from 0 to 100 vol% and relating retained composition to microstructure and mechanical response. The mixed deposits formed dense Al-rich matrices containing dispersed Fe splats, while retained composition deviated from the nominal feedstock composition at higher Fe contents. Porosity decreased from ~0.8% in pure Al to ≤ 0.25% in the mixed deposits, and the flattening ratio of Al splats increased with Fe addition, indicating enhanced matrix deformation. Mechanical properties were governed by retained Fe content: elastic modulus increased from 32 to 61 GPa, while yield/tensile strengths rose from ~40/55 to ~77/94 MPa, approaching saturation beyond ~23–28 vol% retained Fe. Ductility exhibited a non-monotonic trend, reaching a maximum in Al–25Fe (~5% fracture elongation) and decreasing at higher Fe contents as clustering and interface-controlled fracture became more pronounced. Overall, retained composition and spatial distribution governed the balance between strengthening and damage mechanisms, defining an intermediate Fe regime that provides the most favorable mechanical performance.

1. Introduction

Additive manufacturing (AM) has made it easy to produce complex metallic components by enabling geometric freedom, reduced material waste, and functional integration. However, major limitations persist, particularly for multi-material systems. Most established metal AM processes, such as laser powder bed fusion (LPBF), and directed energy deposition (DED) rely on localized melting and rapid solidification, which generate steep thermal gradients and repeated thermal cycles. These conditions promote porosity, solidification cracking, elemental evaporation, residual stress accumulation, and microstructural heterogeneity [1,2]. When extended to dissimilar or multi-material deposits, the mismatch in melting points, thermal expansion coefficients, and diffusion behavior between metals further leads to brittle intermetallic compound formation, delamination, high porosity, microcracks, and thus loss of mechanical integrity, significantly restricting the range of material combinations achievable through fusion-based multi-material AM [3–5]. These challenges bring more attention to solid-state AM techniques capable of reliably producing multi-material metallic structures.

Several solid-state manufacturing approaches have been explored to overcome the limitations associated with fusion-based processing of dissimilar metallic systems. Friction-based technologies, including Additive Friction Stir Deposition (AFSD), Additive Friction Surfacing (AFS), and Friction Stir Additive Manufacturing (FSAM), have demonstrated the ability to produce dense metallic structures while avoiding melting-related defects and enabling the processing of materials that are difficult to combine using conventional fusion-based methods [6–8]. In addition, solid-state joining techniques such as friction stir welding, explosive welding and roll bonding have been successfully employed to fabricate Al–Fe bimetallic structures and other dissimilar material combinations [9–11]. While these approaches offer significant advantages for specific applications, they are often constrained by geometric complexity, feedstock form, build-up rate, or process scalability. Consequently, there remains considerable interest in solid-state additive manufacturing technologies that can provide greater flexibility in material selection, compositional control, scalability and near-net-shape fabrication of multi-material metallic components.

☆ This article is part of a special issue entitled: 'Additive Manufacturing' published in Materials & Design.

* Corresponding author.
E-mail address: sara.bagherifard@polimi.it (S. Bagherifard).

https://doi.org/10.1016/j.matdes.2026.116599
Received 31 May 2026; Received in revised form 3 July 2026; Accepted 15 July 2026
Available online 17 July 2026

In this regard, Cold Spray (CS) has emerged as an alternative due to its low working temperature. CS is a solid-state deposition process where small particles are accelerated to supersonic velocities using a high-pressure pre-heated gas stream before impacting a substrate. The kinetic energy of the particles during impact causes plastic deformation and adhesion via solid-state bonding, resulting in the deposition of dissimilar materials with little interdiffusion, keeping their original compositions [12,13]. In recent years, CS has evolved beyond surface coatings into an AM technology. Cold Spray Additive Manufacturing (CSAM) enables the fabrication of free-standing metal components [14–16] and has also been used for the restoration of damaged metallic parts [17]. Compared to conventional fusion-based AM processes, CSAM offers several advantages, including high deposition efficiency (DE) and build-up rate, unlimited product size, minimal thermal effects, and unprecedented flexibility in material selection [18–23]. Thus, the CS process has been used to produce multi-material deposits, which may involve the combination of metallic materials with different chemical compositions or metallic and ceramic phases [3,24,25].

Considering Al, numerous studies have explored Al-based cold sprayed composites to tailor mechanical and functional properties. Systems such as Al–Cu [26–28], Fe–Al [29–38], Al–Mg [39], Al–Ni [40–42], Al–Sn [43], Al–Ti [44–47], Zn–Al [48,49], and Al–Zr [50] have demonstrated improvements in strength, thermal stability, wear resistance, corrosion protection, and functional performance depending on the secondary phase. These studies highlight the effectiveness of combining Al with a reinforcing phase to exploit its high ductility and DE while enhancing application-specific properties. Among these systems, Al–Fe bimetallic composites are especially attractive because they combine the low density and high thermal/electrical conductivity of Al with the high strength, stiffness, and wear resistance of Fe [51–54]. This combination provides a promising material platform for lightweight structural components requiring tunable stiffness, strength, and damage tolerance. The complementary properties of Al and Fe, together with the ability of cold spray to combine these constituents in the solid state while limiting interdiffusion and phase transformation, have motivated increasing research interest in Al–Fe deposits.

Previous studies have confirmed the feasibility of cold sprayed Al–Fe deposits and have explored several aspects of these systems. Early studies by Wang et al. [29,30] demonstrated the deposition of Al–Fe composite coatings from powder mixtures and investigated phase evolution during post-deposition annealing. Subsequent works employing mechanically alloyed or ball-milled feedstocks focused on the production and characterization of Al–Fe intermetallic coatings, their microstructural evolution, and the influence of post-spray heat treatment [31–34]. More recently, studies have examined the influence of Al–Fe ratio on deposition behavior, microstructural development, corrosion resistance, and tribological performance [35–37], while Palenikova et al. [38] investigated the effect of annealing on Al–Fe thick deposits.

However, a systematic understanding of how the retained phase fraction governs microstructural architecture and tensile mechanical performance remains limited. In particular, relationships between retained composition, splat deformation, local mechanical response, tensile properties, and fracture mechanisms across a broad compositional range have not been established. This gap is critical because the mechanical behavior of cold sprayed bimetallic deposits cannot be inferred directly from nominal powder blending alone, particularly when the constituent phases exhibit markedly different deposition efficiencies and deformation behavior.

Previous Al–Fe studies have employed different feedstock preparation strategies, including premixed, ball-milled, or mechanically alloyed powders [31–34]. In the present work, online powder mixing was used as the selected powder-delivery strategy allowing Al and Fe powders to be blended immediately before injection into the spray jet, and introduced in their as-received state while enabling flexible control of nominal feedstock composition. The purpose of using online mixing here is not to compare it directly with premixed feedstocks, but to examine how retained composition, phase distribution, and defect evolution develop as the Fe content increases.

The present work establishes a composition–structure–property framework for online-mixed Al–Fe composites produced by CSAM. By studying compositions from pure Al to pure Fe, the study maps the translation from nominal feedstock composition to the retained phase fraction in the deposit and relates that evolution to porosity, splat deformation, local hardness, bulk tensile response, and fracture behavior. The central objective is to identify the compositional regime in which Fe addition improves stiffness and strength without causing an unbalanced loss of ductility, thereby providing design guidance for high-performance multi-material CSAM deposits.

2. Materials and methods

2.1. Powder feedstock and its characterization

Commercially available gas atomized pure Al (99.998 wt%) (Toyal Group, FR) and pure Fe (99.64 wt%) (Pometon S.p.A., IT) powders were used in this study. The morphology of powders was examined using Zeiss EVO50 scanning electron microscopy (SEM) (Carl Zeiss microscopy GmbH, DE), as shown in Fig. 1a and b, respectively. Both powders exhibited an intermediate shape between spherical and elongated morphologies. Notably, the Fe powder displayed a more distinct satellite-like structure. To analyze the internal microstructure of the powders, cross-sectional samples were prepared by mounting them in conductive resin, followed by mechanical polishing down to 1 μm. Final vibrational polishing was performed using an oxide polishing suspension (OPS) solution to obtain a better polished surface. Unetched cross-sections of the Al and Fe particles are illustrated in Fig. 1c and d, respectively. Electron backscatter diffraction (EBSD) was conducted on polished cross-sections to characterize the grain morphology within individual particles. EBSD maps were acquired using a Zeiss Sigma 500 SEM with a step size of 0.2 μm and working distance of 10.12 mm. As shown in the inverse pole figure (IPF) maps illustrated in Fig. 1e (Al) and Fig. 1f (Fe), Al particles exhibited several grain-like domains, whereas Fe particles consisted of far fewer grains, typically only one to two. Particle size distribution was measured using a Mastersizer 2000 (Malvern PANalytical Ltd., UK). Al powder exhibited a D10 of 20 μm, D50 of 32.6 μm, and D90 of 53.4 μm, while the Fe powder exhibited a D10 of 17.2 μm, D50 of 26.8 μm, and D90 of 41.3 μm, as plotted in Fig. 2a. While there is a certain difference between the particle size distributions, the overall comparison shows fairly similar behavior in terms of individual and cumulative percentages.

2.2. Cold spray deposition

CS experiments were conducted using an ISS 5/11 high-pressure CS system (Impact Innovations Inc., DE). A convergent-divergent SiC Out-1 nozzle with an expansion ratio of 5.6 was used. CS parameters were selected based on the simulations performed using Kinetic Spray Solution (KSS) software. The simulations incorporated the measured PSD of the Al and Fe powders, along with the corresponding material properties, while maintaining the same spray conditions used in the experiments, including nozzle configuration, stand-off distance (SOD), process gas, and equipment setup. The simulations indicated that both Al and Fe powders fall within their respective deposition windows at process parameters of 450 °C and 50 bar pressure, as depicted in Fig. 2b. The corresponding particle velocity distributions and particle temperature profiles are shown in Fig. 2c and d, respectively. These results provide additional information regarding particle impact conditions achieved under the selected spray parameters and support the process-selection strategy adopted in this work. Nitrogen (N_2) was used as the process gas. The powder mixing was done inside the pre-chamber using two independently controlled powder feeders, which supplied Al and Fe powders separately into the gas stream. The rotating disk speed of each

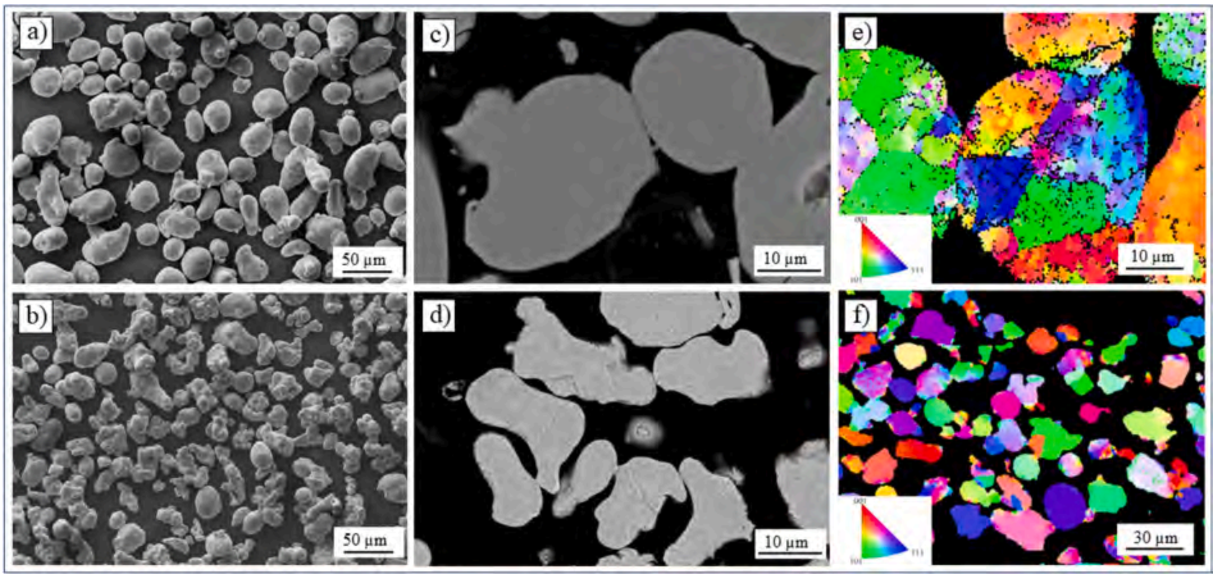

Fig. 1. SEM micrographs analyzing powder particle morphology of a) Al and b) Fe; Cross-sectional micrographs of c) Al and d) Fe; IPF maps of e) Al and f) Fe particles.

feeder was adjusted according to the required Al–Fe feedstock composition, while maintaining a constant combined feeder-disk rotation speed of 6 rpm. Meanwhile, the nozzle transverse speed was set to 250 mm/s with an SOD of 20 mm, and the hatch distance was configured to 1 mm, following a zig-zag scanning pattern.

The relative volumetric proportions of Al and Fe powders were varied from 0% to 100% in the feedstock mixture with 25% steps as detailed in Table 1. An Al6082 alloy substrate was sandblasted with alumina media (54 mesh size) to promote deposit adhesion.

To evaluate the influence of the feedstock composition on the deposit build-up and final composition, deposits were produced under the baseline spray conditions while maintaining consistent transverse speed and hatch distance. Because Fe showed insufficient build-up under the baseline process conditions (450 °C, 50 bar), a higher spray temperature of 900 °C was used for the Fe-only condition (Fe_{900}) to obtain deposits thick enough for bulk mechanical characterization. Fe_{900} was therefore included as a reference condition for pure Fe, whereas all Al-containing deposits were produced under the baseline CS parameters. Consequently, Fe_{900} should therefore not be regarded as a directly comparable endpoint of the compositional series, since differences in deposition temperature may also influence microstructural development and mechanical behavior.

2.3. Microscopical characterization

The deposits were sectioned along their cross-sections and prepared following the same procedure used for the powder cross-sections, for detailed microstructural analysis. SEM imaging of the deposit cross-sections was performed using an EVO50 SEM. Secondary electron (SE) images were used to evaluate the thickness and porosity of the deposits, while backscattered electron (BSE) images were acquired to distinguish between Al and Fe regions based on compositional contrast. ImageJ 1.49 software was employed to quantify the porosity, as well as to analyze phase distribution and retention within the deposits. The retained Fe fraction was quantified from five representative BSE cross-sectional images for each composition using ImageJ image analysis. To validate the phase identification and segmentation procedure, SEM-EDS elemental maps of Al and Fe were acquired for representative deposits and used to verify the spatial distribution of the constituent phases. To quantify the degree of Fe clustering, three representative BSE micrographs of the deposit cross-section were analyzed for each composition using a custom image-processing workflow implemented in Python. Fe-rich regions were segmented from the Al-rich matrix using Otsu grayscale thresholding, followed by morphological filtering to remove isolated noise. Connected Fe-rich regions were identified as individual clusters using connected-component analysis. For each composition, the mean cluster size, maximum cluster size, and nearest-neighbor distance (NND) between cluster centroids were calculated. The NND was determined as the average distance of each cluster centroid from its closest neighboring cluster. To further reveal the splat boundaries, cross-sections were etched using Keller's reagent for Al and Al–Fe deposits, and Nital (5%) solution for Fe deposits. The etching process enhanced the interfaces, allowing for clearer observation of individual splats. The samples were then examined under a Leitz Aristomet optical microscope (OM) to evaluate the microstructural features in more detail. Splat flattening ratio was calculated from microscopic images of well-defined particles with clearly resolved interfaces as an index of the severity of plastic deformation upon particle impact. It was defined as the ratio between the diameter of the circle that completely encloses the splat (d_o) to the diameter of the circle inscribed within the splat (d_i). This definition was inspired by the basic definition, which is based on the width and height of the deformed particle [55].

2.4. Mechanical testing

2.4.1. Nanohardness tests

Nanoindentation measurements were conducted using an Anton Paar 501 (Anton Paar GmbH, DE). A maximum load of 2.5 mN was applied with a loading and unloading rate of 5 mN/min and a dwell time of 5 s. All the tests were performed using a Berkovich indenter at room temperature. Hardness values and Young's modulus (E) were calculated from the load–displacement curves using the Oliver-Pharr method [56]. The nanohardness (H_{IT}) was determined using equation (1):

$$H_{IT} = \frac{F_{max}}{A_p}\# \quad (1)$$

where F_{max} is the maximum applied load and A_p is the projected contact area under the peak indentation load. The indentation modulus was calculated using equations (2) and (3):

$$E_r = \frac{\sqrt{\pi}S}{2\beta\sqrt{A_P(h_c)}}\# \quad (2)$$

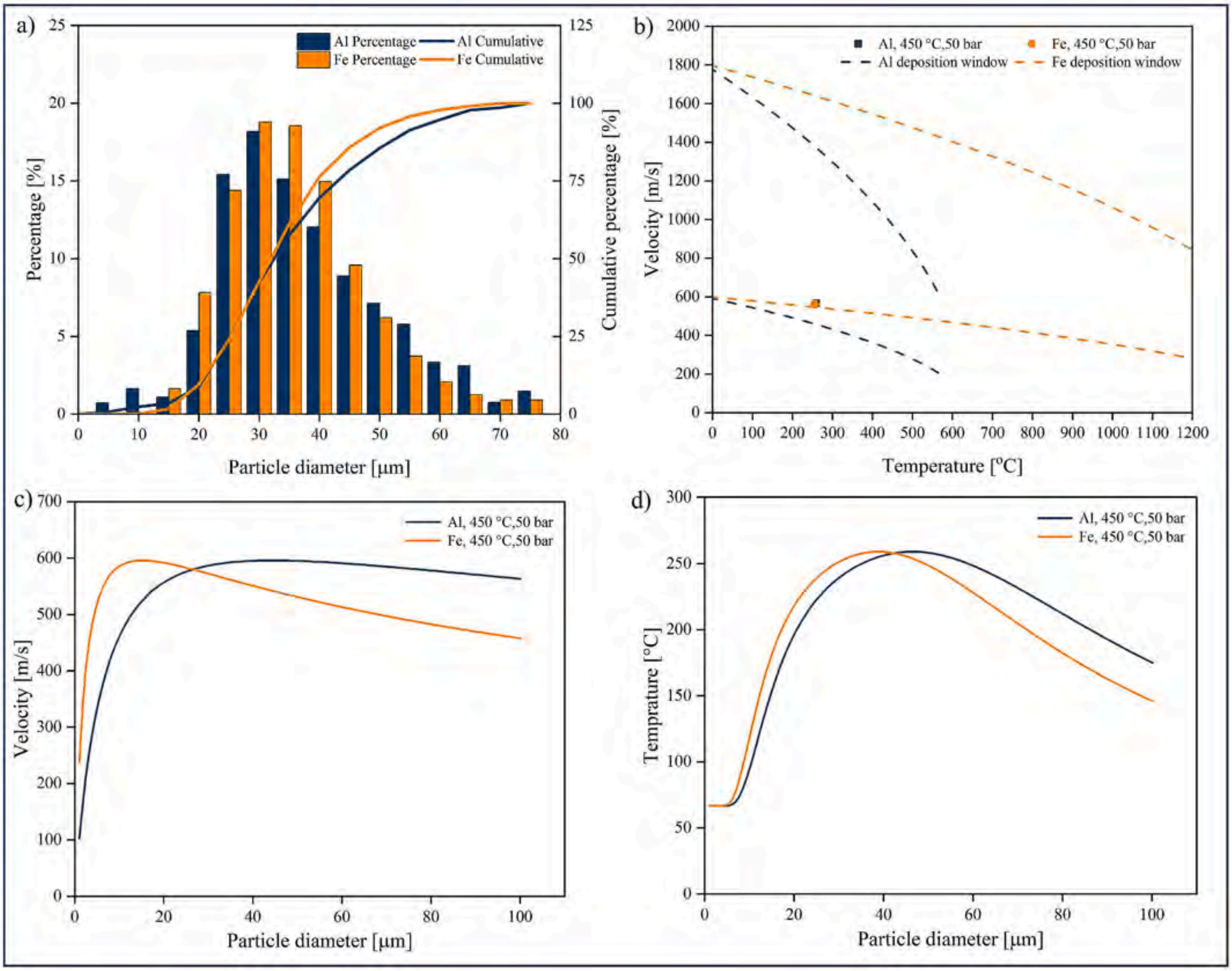

Fig. 2. a) Particle size distribution of Al and Fe powders; results of KSS simulations under the selected CS conditions in terms of b) deposition-window analysis c) predicted particle velocity distributions, and d) predicted particle temperature distributions for Al and Fe powders

Table 1
Feedstock compositions of bimetal deposits.

Sample	Material	Al	Al–25Fe	Al–50Fe	Al–75Fe	Fe
Feedstock volume fraction [%]	Al	100	75	50	25	0
	Fe	0	25	50	75	100

$$\frac{1}{E_r} = \frac{1-v_i^2}{E_i} + \frac{1-v_s^2}{E_s}\# \quad (3)$$

where E_r is the reduced modulus, β is the geometry factor for a Berkovich indenter (1.034), h_c is the contact depth of the indenter, E_s and v_s are the modulus and Poisson's ratio of the specimen, E_i (1141 GPa) and v_i(0.07) are the modulus and Poisson's ratio of the diamond indenter, S is the contact stiffness (dp/dh), where fitting of the load–displacement curve started at 98% of F_{max} and ended at 40% of F_{max}.

A total of 100 indentations were performed on each specimen by considering a matrix pattern to collect detailed data across individual splats as well as along the interface regions. Indents located on pores or those showing irregular behavior were excluded from the analysis to ensure data reliability.

2.4.2. Microhardness tests

Microhardness measurements were performed using an FM-810 Vickers micro-indentation tester (Future-Tech Corp, JP). The measurements were done on powder particles before deposition as well as on the individual splats within the CS deposits, using a 5 gf load with 10 s dwell time, repeating 10 measurements for each series of samples. It was made sure to confine the indentation at the centre of the splat or particle, with a distance at least 2.5 times the indent diagonal from the particle/splat perimeter. The global microhardness of the deposits was measured using a 300 gf load with a 10 s dwell time, with 10 repetitions for each series.

2.4.3. Tensile tests

Sub-size dog-bone flat tensile test specimens, as illustrated in Fig. 3a, were extracted from the deposits along the L-T plane, as shown in Fig. 3b. For each batch, three specimens were extracted perpendicular to the build direction using electrical discharge machining (EDM). To minimize the influence of the substrate on the deposit properties, the specimens were taken 1 mm away from the substrate surface. Tensile tests were performed using a K&W tensile stage (Kammrath & Weiss GmbH, DE) equipped with a 5 kN load cell, integrated within the Zeiss Sigma 500 SEM. The tests were performed under displacement control at a rate of 0.1 μm/s. Two ex-situ tests and one in-situ test were conducted

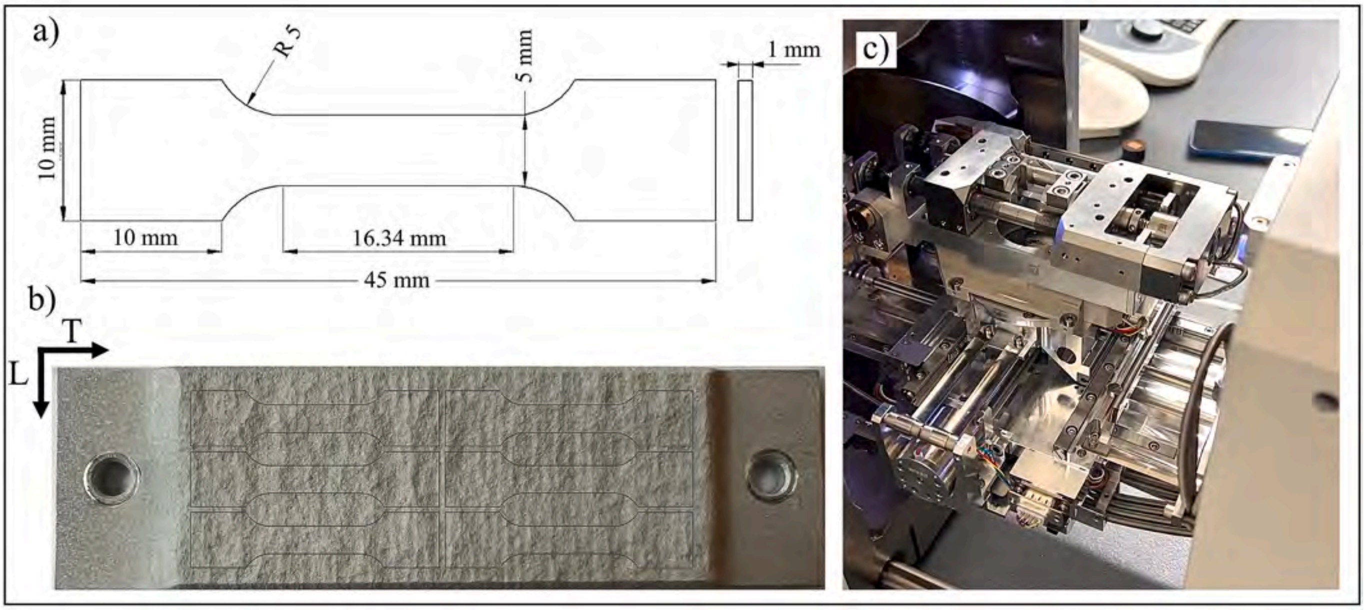

Fig. 3. a) Geometry and dimensions of the tensile test specimens b) Placement of sub-size dog-bone flat tensile specimens within the thick CS deposits. c) In-situ test setup inside the Zeiss Sigma 500 SEM.

for each series. For the in-situ test, the tensile stage was positioned inside the SEM chamber, as shown in Fig. 3c. Prior to testing, the specimen surfaces were ground and finally polished with 1 μm diamond suspension to reveal the splats. During the in-situ test, images were acquired every 15 s to monitor the deformation behavior under tension. Tensile loading was paused upon detecting a load drop to capture high-resolution images at critical moments, allowing for detailed observation of crack initiation and propagation. Both backscattered and SE images were captured at selected intervals. Data extraction was conducted in accordance with EN ISO 6892–1 [57]. Engineering stress was calculated by dividing the applied load by the specimen cross-sectional area of 5 mm^2. Compliance correction was applied based on the equipment calibration guidance, using a correction factor of 0.03 μm/N. The elastic modulus was determined from the slope of the stress–strain curve between stress values corresponding to approximately 10% and 40% of the yield stress, following the recommendations of EN ISO 6892–1. Yield strength (YS) was determined using the 0.2% offset method, while the ultimate tensile strength (UTS) was defined as the maximum engineering stress reached during testing. Elongation was calculated from the displacement relative to the original gauge length. Post-mortem fractographic analysis was performed using the Zeiss EVO 50 SEM to examine the fracture mechanisms.

2.4.4. *Profilometry-based indentation plastometry tests*

Profilometry-based indentation plastometry (PIP) tests were conducted using the PLX-Benchtop equipment (Plastometrex Ltd., UK), an instrument designed for evaluating the mechanical properties of materials through indentation following the ASTM E3499 standard [58]. PIP was used as a complementary mechanical characterization technique because of its ability to estimate compressive stress–strain response from relatively small material volumes without the need for conventional compression specimens [59,60]. This capability is particularly advantageous for situations where specimen extraction can be challenging and local mechanical variations are often important.

The specimens were extracted from deposits and ground up to a P2500 surface finish, ensuring a levelled surface for accurate measurements. Indentation was performed normal to the plane of the samples. Testing was performed using a spherical-tip indenter with a radius of 0.5 mm and at room temperature. Each specimen was subjected to at least three PIP test repetitions to ensure the reliability of the results. PIP characterizes the plastic behavior of materials by applying a controlled load through a hard spherical indenter and then measuring the full residual indentation profile. To extract mechanical properties, the method employs an inverse finite element method (FEM) framework. An indentation simulation is performed using an assumed constitutive law, and the plasticity parameters are iteratively adjusted until the simulated profile matches the measured one. Once convergence is achieved, the optimized stress–strain curve can be used to estimate mechanical properties or to predict material performance under loading conditions. This combined experimental-computational approach enables rapid, geometry-based determination of quasi-static mechanical properties and has been shown to provide reliable results for metallic materials across a wide range of conditions. A comprehensive description of the methodology and its implementation can be found in the review paper by Clyne et al. [61].

3. Results and discussion

3.1. *Deposit microstructure and composition retention*

Cross-sectional BSE-SEM micrographs of the deposits with two layers of deposition are shown in Fig. 4a–e at low magnification for increasing Fe contents. A relatively thick and dense deposit was obtained for Al and the mixed compositions, whereas Fe alone was less successful in producing a thick, defect-free deposit. In the mixed deposits (Al–25Fe, Al–50Fe, and Al–75Fe), Al particles underwent substantial deformation upon impact and formed a dense continuous matrix, while Fe particles (lighter contrast in the BSE images) remained less deformed and were dispersed within the darker Al matrix. Some local non-uniformity in phase distribution was observed through the deposit thickness, particularly in Al–75Fe (Fig. 4d), which may be related to slight variations in feeder-disc alignment during spraying.

The variation in deposit thickness as a function of feedstock composition can give indications on their overall DE. The thickness for two-layer deposits varied markedly with feedstock composition, as shown in Fig. 5a. Thicknesses of approximately 1.85 mm and 0.21 mm were obtained for the Al and Fe deposits, respectively. The much lower thickness of the Fe deposit reflects the limited build-up capability of Fe under the selected process conditions. The Al–25Fe feedstock produced the thickest deposit, with an average thickness of 2.19 mm, slightly

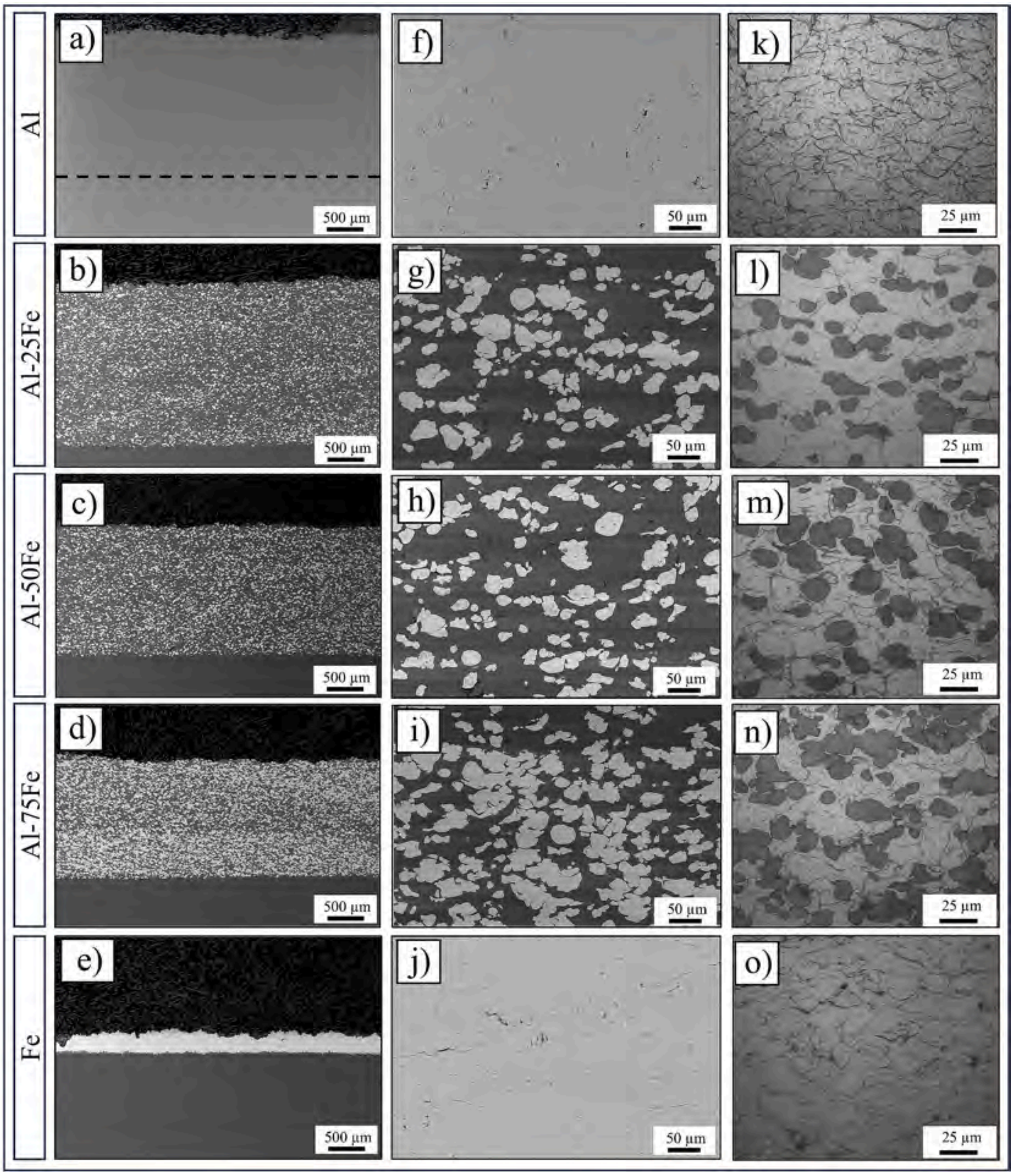

Fig. 4. a–e) Cross-sectional SEM images of Al, Al–25Fe, Al–50Fe, Al–75Fe, and Fe specimens, showing the overall thickness. f–j) Higher-magnification SEM images of Al, Al–25Fe, Al–50Fe, Al–75Fe, and Fe, highlighting detailed morphology and phase distribution across the deposits. k–o) Etched optical micrographs of Al, Al–25Fe, Al–50Fe, Al–75Fe, and Fe deposits, further revealing splat boundaries

higher than that of pure Al. This behavior suggests that the introduction of Fe did not hinder build-up at low Fe contents and may even have promoted deposit growth under these conditions. However, with further increase in Fe content, the thickness decreased to 1.63 mm for Al–50Fe and 1.49 mm for Al–75Fe.

Higher-magnification images of the deposits in Fig. 4f–j show the distribution of Fe within the Al matrix. Representative SEM-EDS elemental maps of Al and Fe are presented in Fig. 6, confirming the phase identification and spatial distribution observed in the BSE micrographs. The elemental maps showed excellent agreement with the phase boundaries identified from the BSE images and therefore validated the ImageJ-based phase segmentation used for retained-composition measurements. The observations indicate that the proportions of Al and Fe in the final deposits did not fully match those in the original feedstock, reflecting the different bonding and retention behaviors of the two constituents under the selected process parameters. The deviation of the deposit composition from that of the starting feedstock was assessed from the areal fractions measured on cross-sectional BSE images (see Fig. 5b). The deposit produced from the Al–25Fe feedstock exhibited an Fe content of 23.0%, which is close to the nominal feedstock composition. With increasing Fe content in the feedstock, the retained Fe fraction in the deposit decreased progressively. For the Al–50Fe feedstock, the resulting deposit contained an average of 28.7% Fe, indicating substantially lower Fe retention relative to the nominal composition. This trend became even more pronounced for the Al–75Fe feedstock, where the deposit contained only 45.4% Fe.

For deposits with lower Fe contents, such as Al–25Fe and Al–50Fe (Fig. 4g and h), Fe particles were distributed relatively uniformly throughout the Al matrix, with only limited clustering. In contrast, the Al–75Fe deposit exhibited localized Fe agglomeration or clustering. To quantify this observation, an image-based clustering analysis was performed on representative BSE micrographs, and the results are summarized in Table 2. The corresponding image-analysis workflow is presented in Fig. 7. Fig. 7a–c shows the representative BSE micrographs

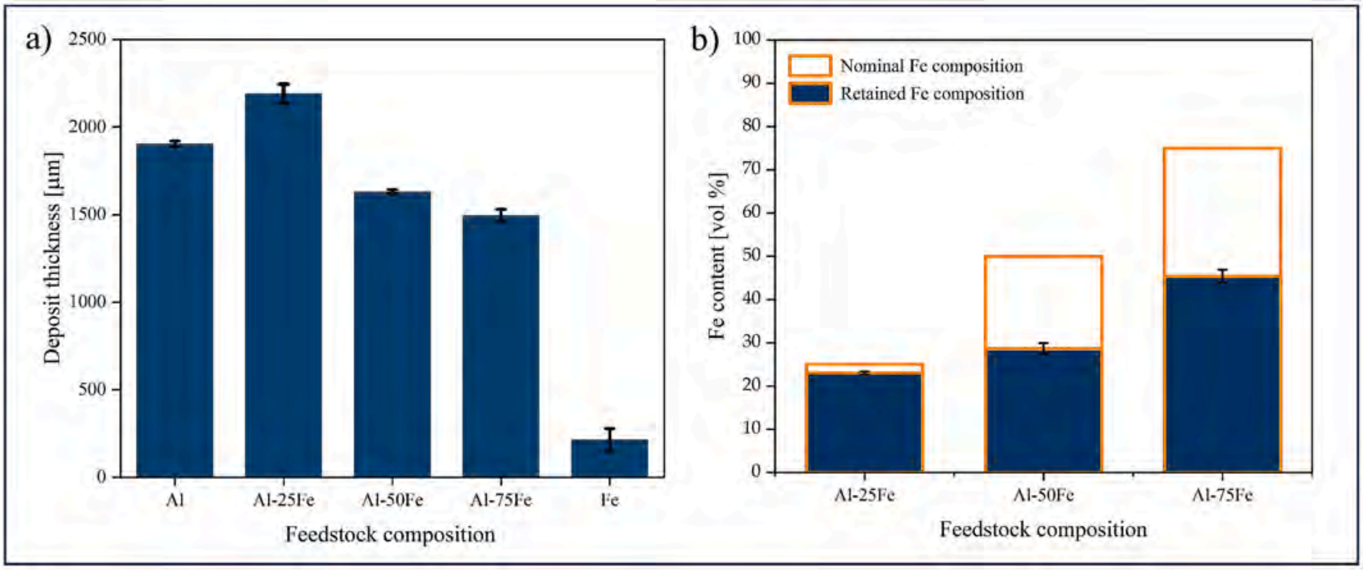

Fig. 5. a) Average thickness of the two-layer deposits b) retained Fe content in the mixed deposits

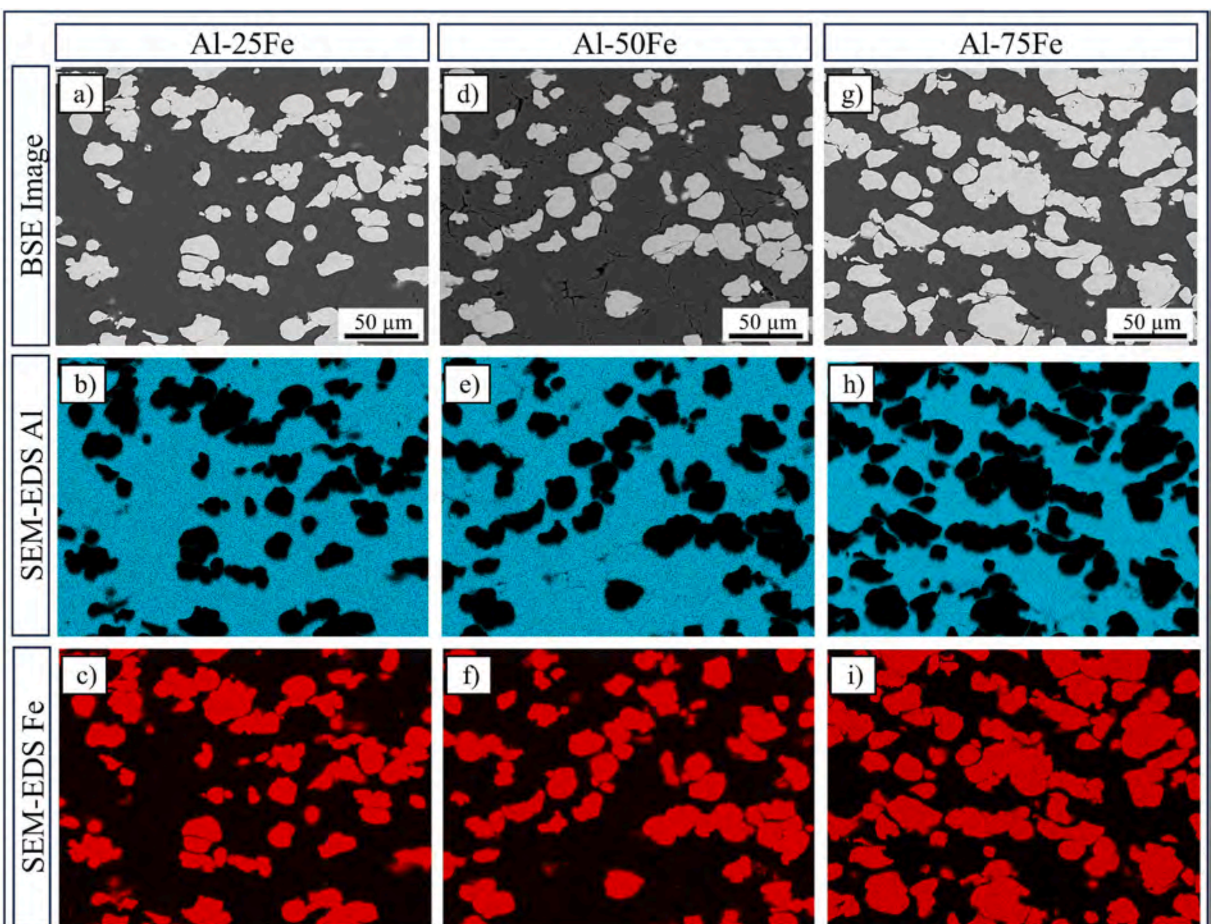

Fig. 6. Representative SEM-BSE images and corresponding SEM-EDS elemental maps in the mixed Al–Fe deposits: a–c) Al–25Fe, d–f) Al–50Fe, and g–i) Al–75Fe. For each composition, the panels show the BSE image, Al elemental map, and Fe elemental map, respectively.

of the Al–25Fe, Al–50Fe, and Al–75Fe composites, respectively. The corresponding cluster maps are shown in Fig. 7d–f, where each connected Fe-rich region identified by connected-component analysis is assigned a unique color and treated as an individual cluster. Red markers indicate the cluster centroids, while green lines represent the nearest-neighbor connections used for NND measurements. The results indicate that mean cluster size increased from 300.8 μm^2 for Al–25Fe to 344.1 μm^2 for Al–50Fe and 680.6 μm^2 for Al–75Fe, indicating

Table 2
Quantitative analysis of Fe-rich clustering in mixed Al–Fe deposits.

Composition	Mean cluster size [μm^2]	Maximum cluster size [μm^2]	NND [μm]
Al–25Fe	300.8 ± 11.1	3085.6 ± 756.1	23.1 ± 0.7
Al–50Fe	344.1 ± 20.2	4226.1 ± 970.5	22.6 ± 0.4
Al–75Fe	680.6 ± 90.8	26744.4 ± 5917.1	22.5 ± 0.9

progressive coarsening of the Fe-rich regions. An even more pronounced trend was observed for the maximum cluster size, which increased from 3085.6 μm^2 to 4226.1 μm^2 and ultimately to 26744.4 μm^2 by increasing Fe content, demonstrating the formation of substantially larger and more interconnected Fe-rich agglomerates in the Al–75Fe deposit. In contrast, the average NND remained within a relatively narrow range of 23.1–22.5 μm across all compositions, indicating that the dominant microstructural change is not a significant reduction in inter-cluster spacing, but rather the growth and coalescence of existing Fe-rich regions into larger clusters. These quantitative results therefore confirm that clustering is primarily characterized by cluster coarsening and the emergence of large Fe-rich agglomerates with increasing retained Fe content. This change in distribution is likely associated with the increased frequency of Fe–Fe particle interactions at higher Fe contents, together with the reduced amount of Al matrix available to separate and accommodate the Fe phase.

The flattening ratios of Al and Fe splats in different deposits were evaluated from the etched cross-sectional micrographs shown in Fig. 4k–o, and the results are summarized in Table 3. The relatively large scatter in the flattening-ratio measurements reflects, at least in part, the irregular morphology of the feedstock particles. Therefore, the calculated flattening ratio should be interpreted primarily as an indicator of the overall deformation trend rather than as an absolute measure of particle deformation. The flattening ratio of Al splats increased progressively with increasing Fe content in the feedstock. In contrast, the flattening ratio of Fe splats remained relatively unchanged, or decreased slightly, across the mixed deposits. In the pure Fe deposit, however, the Fe flattening ratio nearly doubled. This indicates that Fe particles experienced substantially greater deformation when interacting predominantly with other Fe particles than when embedded in the softer Al matrix. In the mixed deposits, the Fe splats exhibited reduced flattening response since their interactions with the softer Al splats were more frequent, which limited the extent of their deformation. Direct comparison between Al and Fe should be made with caution because the two powders differed in both initial morphology and particle size distribution. In the mixed deposits, Al splats consistently displayed greater flattening than Fe splats, which is consistent with their higher plasticity and lower hardness.

The porosity values of the deposits, determined by quantitative image analysis of the SEM micrographs in Fig. 4f-j, are summarized in Table 3. The Al deposit exhibited a porosity of approximately 0.8%. Introducing Fe into the Al feedstock reduced the porosity further, lowering it to below 0.25% in all mixed deposits. In contrast, the Fe deposit showed a porosity of 1.36%. This comparatively high porosity is consistent with the limited plastic deformation of Fe particles, which restricts particle flattening and efficient pore closure upon impact. Overall, all deposits except Fe exhibited porosity levels below 1%, indicating the formation of dense deposits.

Upon impact, four different particle-interaction types can occur, namely Al–Al, Al–Fe, Fe–Al, and Fe–Fe, and the retained composition of the deposit reflects the combined outcome of these individual interaction-dependent DEs. Although DE was not measured directly in this study, KSS simulations were used to estimate the deposition behavior for the Al–Al and Fe–Fe cases using the selected process parameters and the experimentally measured particle size distributions. The simulations yielded estimated DEs of 95% for Al–Al and 62% for Fe–Fe. The progressive decrease in Fe retention with increasing Fe content in the feedstock is therefore consistent, at least in part, with the lower DE of Fe–Fe interactions under the present conditions. The decrease in the deposit thickness across the mixed compositions is

Table 3
Flattening ratio calculated for the Al and Fe splats and porosity levels of pure and mixed deposits.

Composition	Al	Al–25Fe	Al–50Fe	Al–75Fe	Fe
Porosity	0.8 ± 0.12	0.25 ± 0.04	0.24 ± 0.04	0.16 ± 0.03	1.36 ± 0.32
Flattening ratio, Al	2.9 ± 1.3	3.7 ± 1.6	4.1 ± 2.4	4.5 ± 2.6	–
Flattening ratio, Fe	–	2.4 ± 1.4	2.3 ± 1.4	2.1 ± 0.7	4.3 ± 2.0

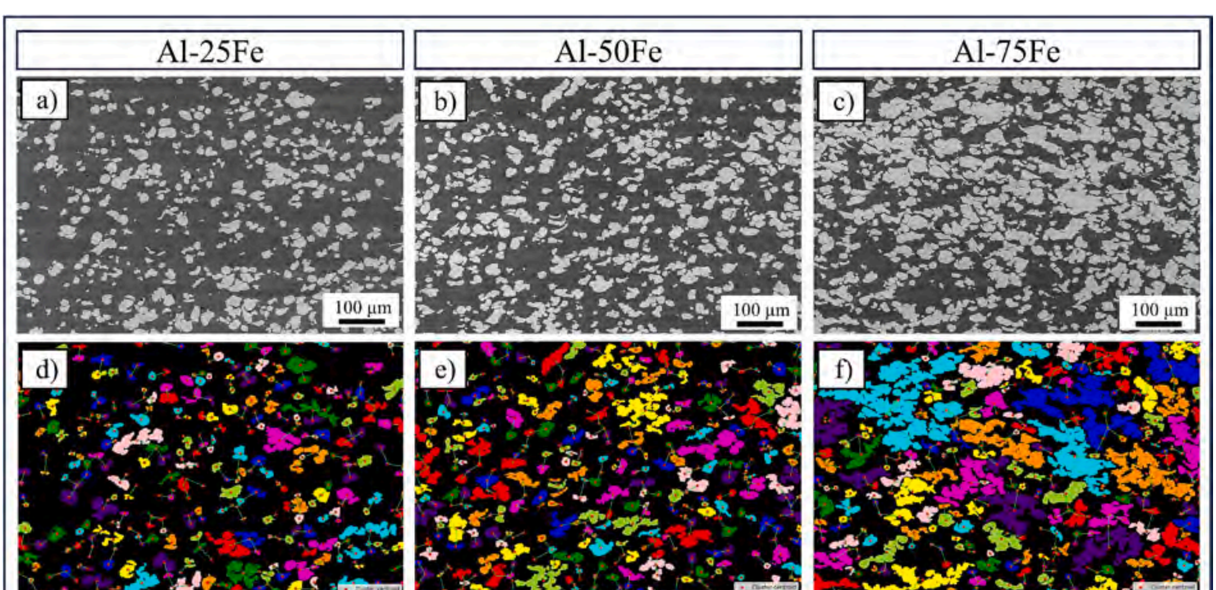

Fig. 7. Representative BSE micrographs (a–c) and corresponding Fe-rich cluster maps with NND analysis (d–f) for Al–25Fe, Al–50Fe, and Al–75Fe composites.

expected, considering the low DE of Fe–Fe interactions as well as the flattening ratios of individual phases.

3.2. Indentation-based mechanical response

Nanoindentation was performed to resolve the local mechanical response of individual splats and interfacial regions, which cannot be distinguished by bulk mechanical testing alone. This analysis is important for understanding how Fe incorporation modifies splat-scale hardness, stiffness variation, and local mechanical heterogeneity, thereby linking the observed microstructural architecture to the global mechanical response. Fig. 8 shows the indentation matrix together with the corresponding hardness heat maps. For the Al and Fe deposits, the nanohardness was relatively uniform over the mapped areas, consistent with their comparatively homogeneous microstructures. In contrast, the mixed deposits exhibited clear spatial variations in hardness, with higher values associated with Fe-rich regions and lower values associated with Al-rich regions. In the Al–Fe composites, the transition between soft and hard regions was captured by the heatmaps, showing a gradual increase in hardness from the Al matrix toward Fe splats. The hardness measured at the interfacial regions appeared intermediate between the values of Al and Fe. These values should be interpreted with caution, as the measured interfacial response is dependent on the exact indentation location and may be biased by the local phase distribution, reflecting a dominant contribution from either the Fe or Al phase.

The average nanohardness values of the deposits and the corresponding powder particles (shown as dashed lines), together with the indentation modulus values and their standard deviations, are presented in Fig. 9. The hardness of Al splats in the Al deposit (485 MPa) was approximately 8.6% lower than that of the original Al powder particles (531 MPa). This reduction is consistent with thermal softening during deposition, which may promote recovery and recrystallization and thereby reduce the effect of prior work hardening [62,63]. Such work softening can occur in extra-pure Al, since the recovery and recrystallization temperatures decrease markedly with increasing purity [64,65]. With increasing Fe content, the nanohardness of Al splats progressively increased, reducing the difference between the deposited splats and the original powder.

In contrast, the nanohardness of Fe splats remained relatively stable within the mixed deposits, with values around 2300 MPa. A higher hardness, approximately 2959 MPa, was measured in the pure Fe deposit, corresponding to an increase of about 28% relative to the mixed conditions. This trend is consistent with stronger strain hardening in the Fe-only deposit, where repeated Fe–Fe impacts dominate and interactions with the softer Al phase are absent. Across all mixed deposits, Fe splats exhibited higher hardness than their corresponding powder particles (1899 MPa), indicating that work hardening during impact remained more influential than any possible thermal softening under the selected cold spray conditions. As the Fe content in the feedstock increased, the hardness measured in regions close to Al–Fe boundaries also increased, reaching values up to 1456 MPa. This trend is consistent with increasing local mechanical constraint and deformation heterogeneity in the mixed deposits.

The indentation modulus results are shown in Fig. 9b. These data reflect the local elastic response under indentation and provide an indication of stiffness at the splat scale. The measured modulus of Al splats increased from approximately 68 GPa in the Al deposit to around 77 GPa in the Al–25Fe and Al–50Fe deposits, and further to about 85 GPa in the Al–75Fe deposit. A similar increasing trend, accompanied by considerable scatter, was also observed for Fe splats. In both materials, the relatively large standard deviations can be attributed primarily to crystallographic anisotropy. Because individual splats often contain only a limited number of grains, nanoindentation may probe regions with different crystallographic orientations, resulting in orientation-dependent variations in the measured elastic response. Such effects have been reported previously for both Al and Fe single crystals [66,67]. In addition, local residual stresses [68] and the reduced porosity of the mixed deposits [69] may also contribute to the observed increase in indentation modulus, although these effects cannot be isolated directly in the present study.

In addition to nanoindentation, microhardness testing was performed to obtain a more representative global measure of the mechanical response of the Al–Fe deposits. Microhardness measurements were carried out both at the deposit level, where several splats contribute to the response, and within individual Al and Fe splats using a lower indentation load. The local splat-level values are shown as dashed lines together with the deposit-level microhardness data in Fig. 10. Overall, the microhardness trends follow those observed in nanoindentation. For instance, the average microhardness of Al splats in the Al deposit (24.3 HV) was lower than that of the Al powder particles (37.7 HV). The hardness of Al splats increased progressively with increasing Fe content, reaching 40.7 HV in the Al–75Fe deposit. Fe splats, on the other hand, consistently exhibited substantially higher hardness values, ranging from 150 HV to 211 HV, owing to the intrinsically higher hardness and lower deformability of Fe.

The main difference observed between the local and global microhardness values for both Al and Fe deposits was that in the Al deposit, the global microhardness was approximately 15.5% higher than the

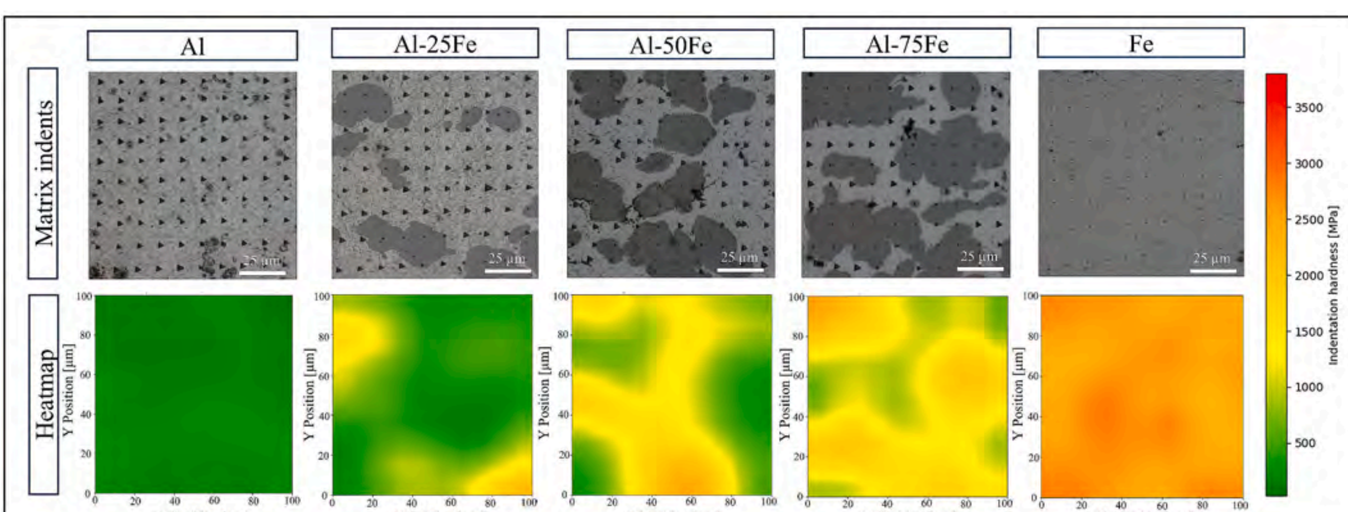

Fig. 8. Nanoindentation hardness maps of all the deposits.

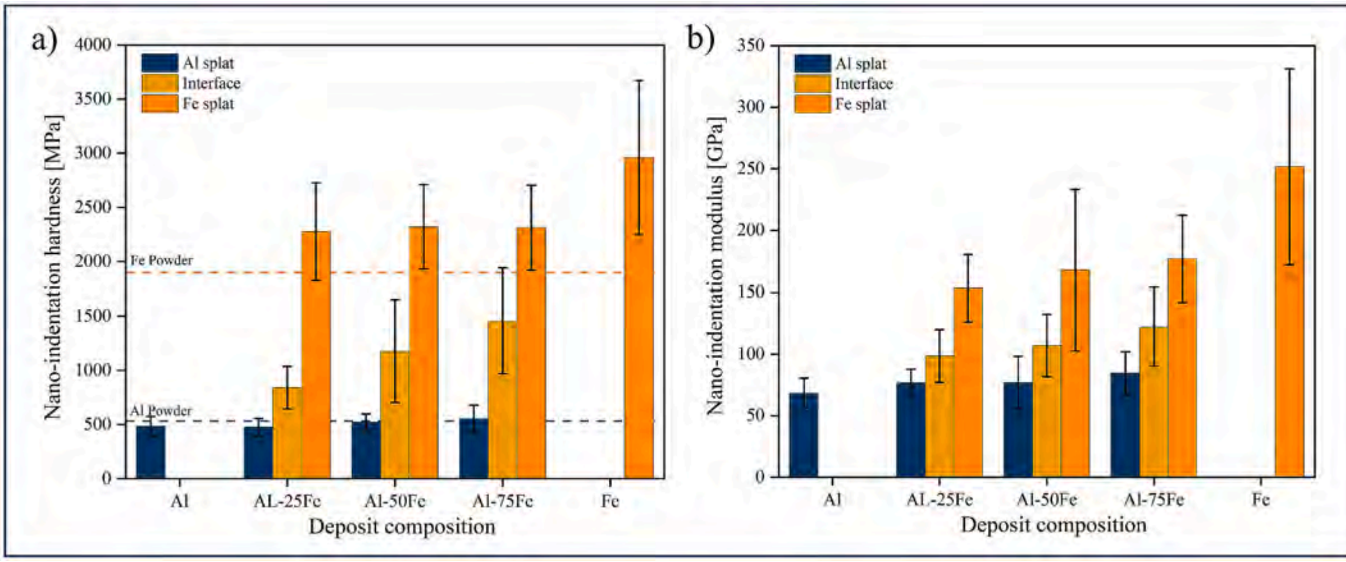

Fig. 9. a) Nano-indentation hardness b) nano-indentation modulus of Al–Fe bimetallic deposits

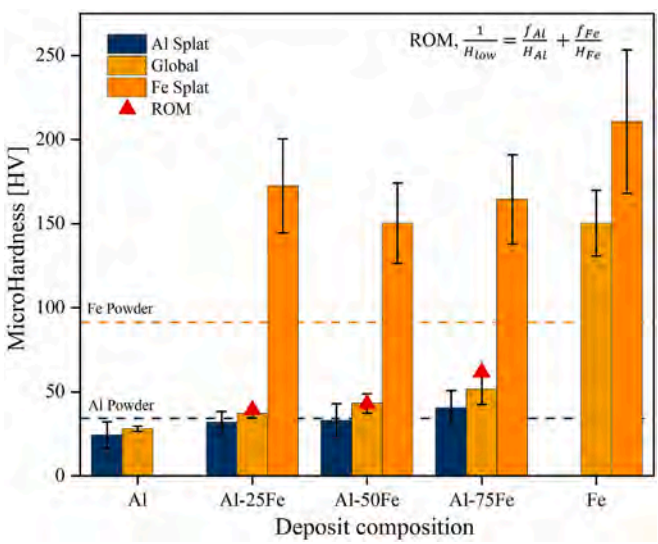

Fig. 10. Vickers microhardness measurements for individual splats and overall deposits. For comparative purposes, rule of mixtures (ROM) values are also included.

hardness of individual Al splats. In contrast, the global microhardness of the Fe deposit was about 28.6% lower than the corresponding Fe splat hardness. In the Fe deposit, the larger indentation volume associated with global microhardness measurements is more likely to include cracks, pores, and inter-splat defects, which reduce the apparent hardness, while in the Al deposit, the density of these defects would be less. The different length scales sampled by the two measurements, known as the indentation size effect, could have also contributed to this discrepancy. As the Fe content increased in the mixed deposits, the global microhardness also increased, in agreement with the increasing fraction of the hard Fe phase.

To assess whether the hardness of the mixed deposits could be approximated using a simple rule of mixtures (ROM) approach, the experimental deposit-level microhardness values were compared with lower-bound predictions based on the iso-stress model [70]. The corresponding equation is given in Fig. 10, where H_{low} is the predicted lower-bound hardness, H_{Al} and H_{Fe} are the splat-level hardness of the Al and Fe phases, and f_{Al} and f_{Fe} are their respective volume fractions. The experimentally measured global microhardness values remain close to, but generally below, the ROM predictions. It should be noted that the hardness measurements at the splat and global scales may be influenced by indentation size effects, which could partially justify the mismatch between experimental data and ROM predictions. A lower global hardness could also be attributed to the microstructural features inherent to the CS deposits, including incomplete inter-splat bonding, and local porosity. Therefore, while the ROM provides a useful first-order reference, it does not fully capture the mechanical response of the present heterogeneous deposits.

3.3. Tensile test results

Fig. 11 shows representative engineering stress–strain curves obtained from tensile tests of the different deposits, while Table 4 summarizes the corresponding mechanical properties. The reported values were determined from three tensile tests performed for each composition, comprising two ex-situ tests and one in-situ SEM tensile test. A clear

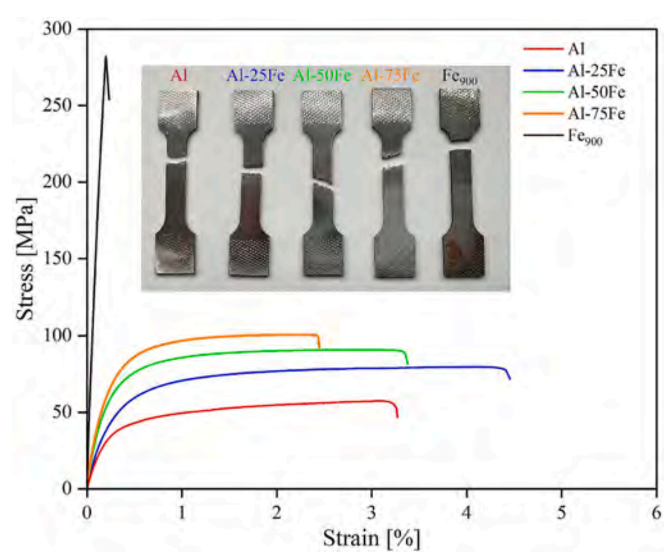

Fig. 11. Representative engineering stress–strain curves of various deposits (Fe_{900} was produced at a higher deposition temperature (900 °C) and is included as a reference condition for pure Fe.)

Table 4
Uniaxial tensile mechanical properties for various deposits.

Composition	Al	Al–25Fe	Al–50Fe	Al–75Fe	Fe_{900}
Elastic Modulus [GPa]	32.1 ± 2.9	45.8 ± 5.6	55.5 ± 3.0	61.1 ± 2.1	184.2 ± 15.7
Yield strength [MPa]	39.7 ± 1.6	58.9 ± 1.9	76.4 ± 3.5	77.2 ± 3.1	–
Tensile strength [MPa]	55.2 ± 3.0	80.6 ± 0.8	93.8 ± 2.9	94.0 ± 9.5	270.5 ± 11.2
Uniform Elongation [%]	2.3 ± 1.1	4.3 ± 0.3	2.6 ± 0.4	1.9 ± 0.6	0.2 ± 0.01
Elongation at fracture [%]	2.5 ± 1.1	4.7 ± 0.1	3.1 ± 0.3	2.1 ± 0.5	–

increase in the tensile modulus of the deposits was observed with increasing Fe content, rising from 32 GPa for Al to approximately 61 GPa for Al–75Fe. This increase is consistent with the intrinsically higher stiffness of Fe relative to Al. As the Fe fraction increased, the macroscopic tensile response of the composite deposits became progressively stiffer. Nevertheless, the modulus values of the mixed deposits remained much closer to that of Al than to that of Fe, indicating that the overall elastic response was still governed primarily by the Al-rich

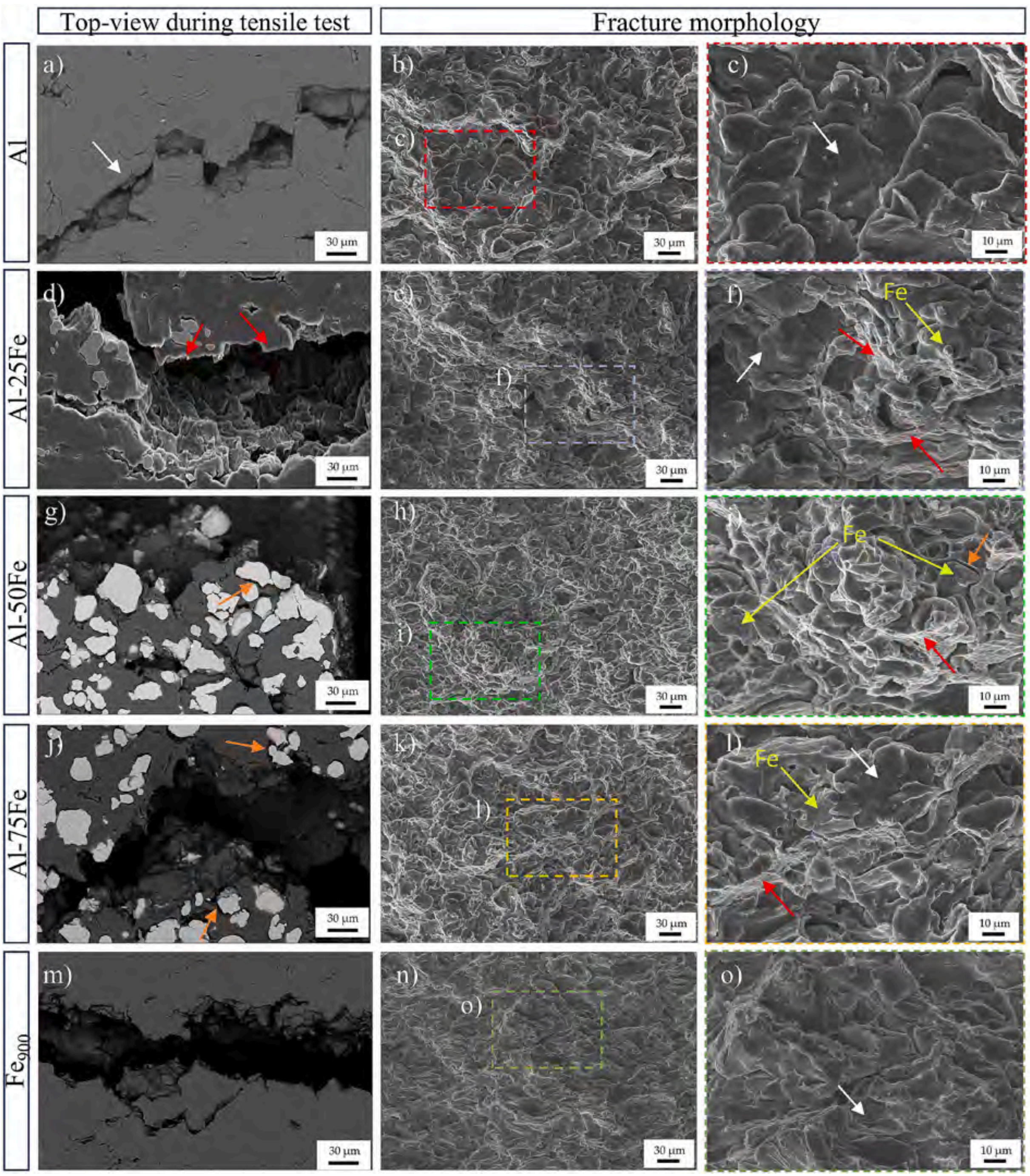

Fig. 12. Lateral SEM observations during tensile test, corresponding fracture surfaces, and higher-magnification views of the fracture surfaces for a–c) Al, d–f) Al–25Fe, g–i) Al–50Fe, j–l) Al–75Fe, and m–o) Fe_{900} specimens

matrix and by the deposit architecture. Because sufficient bulk build-up could not be achieved for Fe at 450 °C, a direct tensile modulus could not be obtained for that condition. For reference, the Fe_{900} deposit, produced at 900 °C to enable adequate build-up, exhibited a tensile modulus of 184 GPa.

Similar to the elastic modulus, both YS and UTS increased with increasing Fe content in the Al-based deposits, as shown in Table 4. The Fe_{900} reference exhibited a tensile strength of about 270 MPa, without a distinct yield point because fracture occurred with essentially no measurable plastic region. In the mixed deposits, the increase in strength is consistent with the reinforcing contribution of the Fe phase within the Al matrix. The most pronounced improvement occurred at low-to-intermediate Fe contents. Relative to Al, the YS increased by 48% for Al–25Fe and by 92% for Al–50Fe, but only by 94% for Al–75Fe. The corresponding trends in E and UTS followed a similar pattern, indicating that strengthening tended to saturate beyond an intermediate retained Fe content.

Ductility, evaluated in terms of uniform elongation and elongation at fracture, exhibited a non-monotonic dependence on composition, as shown in Table 4. The Al deposit displayed moderate ductility, with an elongation at fracture of 2.5%. This value is higher than those reported in some earlier studies on cold sprayed Al, for example, below 1% for Al deposited at 350 °C and 17 bar [71], and about 0.2% for Al deposited at 380 °C and 30 bar [72]. The comparatively higher ductility observed in the present study may be associated, at least in part, with the higher gas temperature and pressure, which likely promoted improved particle deformation, inter-particle bonding, and a lower density of critical interfacial defects.

Among all compositions, the Al–25Fe exhibited the highest ductility, with a fracture elongation of 4.7%. With further increase in Fe content, however, the elongation decreased again, reaching 3.1% for Al–50Fe and 2.1% for Al–75Fe. This indicates that an intermediate Fe content provides the most favorable balance between strengthening and ductility. In contrast, the Fe_{900} reference exhibited extremely limited tensile ductility, with an elongation at fracture of only 0.2%. Such behavior is typical of as-sprayed deposits of high-strength materials, where limited plastic deformability and incomplete inter-splat bonding promote early fracture.

3.4. Fractography and tensile failure mechanisms

Fig. 12 presents lateral SEM micrographs together with the corresponding fracture-surface morphologies for all the investigated compositions. Overall, the fracture behavior evolved systematically with composition, reflecting a gradual transition from predominantly inter-splat, brittle fracture in Al to more complex mixed-mode fracture in the Al–Fe composites, and finally to catastrophic brittle failure in Fe_{900}. In all specimens, crack initiation was observed mainly along inter-splat boundaries, underscoring the critical role of these interfaces in controlling tensile failure in cold sprayed deposits.

For the pure Al specimen (Fig. 12a–c), crack propagation occurred largely along relatively planar inter-splat boundaries, producing smooth fracture surfaces with flat facets. These features indicate limited plastic deformation during failure and are consistent with predominantly brittle fracture controlled by weak inter-splat cohesion. The weakly bonded interfaces are believed to be a primary cause of strain localization and premature failure in the as-sprayed condition of CS samples [73,74]. A comparatively large scatter in the elongation of Al samples (Table 4) further indicated the stochastic nature of damage initiation likely resulting from a higher density of internal defects in this deposit.

The incorporation of Fe in the Al–25Fe deposit (Fig. 12d–f) modified the crack path significantly. Dispersed Fe particles appeared to act as local obstacles to crack propagation, promoting crack deflection and forcing the advancing crack to deviate around the harder Fe splats. Such behavior is consistent with local strain redistribution and improved resistance to straight-through interfacial fracture [67]. Fracture in this composition involved a combination of interfacial debonding and ductile tearing of the Al matrix. Evidence of matrix tearing is visible in Fig. 12e and is highlighted more clearly at higher magnification in Fig. 12f (red arrow), indicating a greater contribution from ductile deformation than in the pure Al deposit. Nevertheless, some locally planar regions are still present, suggesting that weakly bonded splat interfaces remained active in part. Compared with the pure Al deposit, however, the greater contribution from matrix tearing indicates a higher degree of local plastic deformation prior to failure.

With further increase in Fe content, the fracture behavior became progressively more complex and increasingly brittle. In the Al–50Fe deposit (Fig. 12g–i), the higher Fe fraction produced denser Fe-rich regions and a larger number of potential crack-initiation sites. Crack propagation was frequently associated with Al–Fe interfaces, and the fracture surface exhibited a mixed morphology, combining localized dimples (Fig. 12i, red arrow) with more brittle features. This indicates that Al–50Fe represents a transitional condition in which some local plastic deformation is still retained, but interfacial decohesion becomes increasingly important.

In the Al–75Fe deposit (Fig. 12j–l), the Fe-rich regions became larger and more interconnected, and the fracture mode shifted further toward interface- and particle-dominated failure. Cracks preferentially initiated or propagated in Fe-rich zones and along Al–Fe interfaces, where stress concentrations and local discontinuities were more pronounced. The fracture surfaces displayed clear evidence of particle pull-out (orange arrows) together with brittle trans-particle fracture features in Fe-rich regions (green arrow). Compared with Al–50Fe, the contribution from ductile tearing of the Al matrix was further reduced, and the fracture response was dominated more strongly by interfacial debonding and brittle crack propagation through the reinforcement-rich microstructure.

The Fe_{900} specimen, produced at 900 °C to enable sufficient build-up, exhibited immediate and catastrophic crack propagation under tensile loading, with virtually no measurable plastic deformation. As shown in Fig. 12m, cracks propagated almost directly through splat interfaces, which displayed signs of incomplete bonding and predominantly brittle fracture. The corresponding fracture surface, shown in Fig. 12n and o, was relatively flat and featureless and lacked significant evidence of ductile dimpling, which is consistent with cleavage-like brittle failure.

3.5. Profilometry-based indentation plastometry (PIP)

PIP was employed as a complementary mechanical characterization method to examine the response of the deposits under constrained plastic deformation. In contrast to uniaxial tensile loading, the PIP method is based on a predominantly compressive, triaxial stress state beneath the spherical indenter. As a result, it is less sensitive to crack opening and interfacial decohesion under tension, and therefore provides a different perspective on the deformation behavior of the deposits. This distinction is particularly relevant for cold sprayed heterogeneous materials, in which premature tensile failure is often strongly influenced by splat interfaces and local defects.

The PIP-derived nominal stress–strain curves for the different deposits are shown in Fig. 13, and the corresponding YS and UTS values are summarized in Table 5. For comparison, values reported for cold-rolled Al and Fe are also included. For these reference materials, the PIP-derived strengths show reasonably good agreement with the corresponding literature data, supporting the applicability of the method to the present material system. A clear increase in flow stress was observed with increasing Fe content. Both YS and UTS derived from the PIP analysis increased progressively from Al to Al–75Fe, consistent with the strengthening trend also observed in the uniaxial tensile tests. In

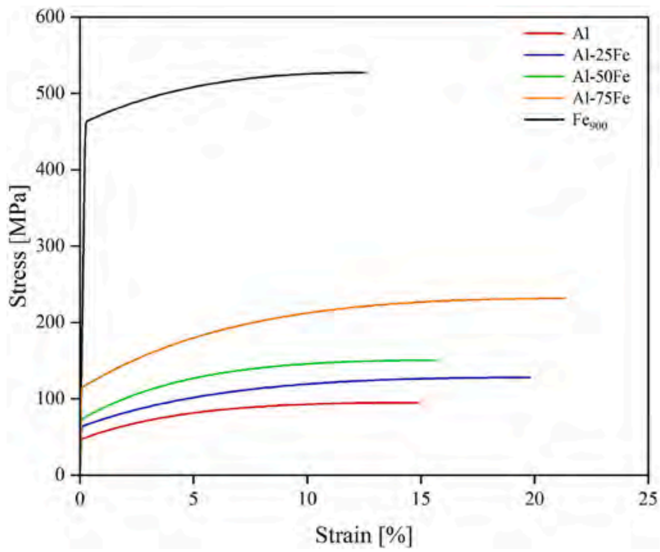

Fig. 13. Representative engineering stress–strain curves derived from PIP test.

addition, the strain capacity inferred from the PIP curves was substantially high, with values reaching approximately 15–20% in the mixed deposits. The Al–Fe composite deposits also maintained strain capacity comparable to, or in some cases greater than, that of the Al deposit under the present PIP conditions.

4. Discussion

4.1. Composition-dependent deposition behavior and microstructural evolution

The incorporation of Fe into Al clearly modified both the deposition behavior and the resulting microstructure of the deposits. Under the selected process conditions, Al exhibited a good build-up rate, whereas Fe alone showed much more limited build-up capability. As a result, the mixed deposits displayed intermediate behavior between these two. In particular, Fe retention was more favorable at low Fe contents, while progressively lower retained Fe fractions were obtained as the nominal Fe content in the feedstock increased.

To the best of the authors' knowledge, no previous study has directly compared online-mixed and premixed Al–Fe feedstocks under identical cold spray conditions. Therefore, the relative influence of the powder-delivery strategy itself on Fe retention, compositional homogeneity, or mechanical response cannot currently be isolated or quantified from the available literature. Nevertheless, previous studies on cold-sprayed Fe–Al systems have employed various powder preparation strategies, which provide useful context for interpreting the present results. Mechanical mixing [35,38] and short-duration high-energy ball milling [29,30] generally preserve the original powder microstructure and have been reported to produce deposits with macroscopically homogeneous Al–Fe distributions governed largely by particle deformation during impact. In these cases, Al deforms readily to form a dense matrix, whereas Fe remains less deformed and is dispersed within it, resulting in microstructural features broadly similar to those observed in the present work. However, such premixed systems may still be affected by powder segregation, and oxidation during handling and feeding, which can influence the final retained composition and deposit homogeneity. In addition, prolonged high-energy ball milling or mechanical alloying [31–34] fundamentally alters the feedstock prior to deposition by introducing severe plastic deformation, strain hardening, and in some cases lamellar or mechanically alloyed internal structures that are subsequently inherited by the deposited coating. Although such approaches can enhance microstructural refinement, they may also modify the initial particle morphology and deformability, thereby making it more difficult to isolate the effects of deposition itself from those introduced during powder pre-processing.

In the present study, online mixing was used as the selected powder delivery strategy. Its role was to vary the feedstock ratio while preserving the as-received characteristics of the Al and Fe powders, thereby avoiding additional modifications associated with powder preprocessing. This allowed the present work to focus on how the nominal feedstock composition is translated into retained Fe content and how the retained composition governs the resulting microstructural architecture and mechanical response. This relationship is reflected in the progressive deviation between nominal and retained Fe content as the feedstock Fe fraction increases, together with the corresponding evolution in matrix continuity, Fe clustering, and porosity. The microstructural trends observed in Section 3.1 are consistent with this interpretation. At low Fe contents, the deposits retained Fe fractions close to nominal and exhibited relatively uniform Fe dispersion within a dense Al matrix. With increasing Fe content, however, the retained Fe fraction deviated increasingly from the nominal feedstock composition, while localized Fe clustering became more evident. This behavior is consistent with the increasing frequency of Fe–Fe interactions at higher Fe contents, together with the comparatively lower estimated DE for Fe–Fe impacts under the selected conditions.

Overall, the present results show that the deposition behavior of online-mixed Al–Fe feedstocks cannot be described solely by the nominal powder ratio. Instead, the final deposit architecture is governed by the interaction between nominal composition, constituent-specific retention behavior, and the evolving local impact environment during build-up. This distinction is important because it highlights that retained composition, rather than nominal feedstock composition alone, provides a more relevant basis for interpreting the resulting microstructure and, ultimately, the mechanical behavior of the deposits.

4.2. Composition-dependent mechanical response of Al–Fe deposits

The incorporation of Fe into Al had a pronounced effect on both microstructural evolution and the mechanical response of the deposits. The most immediate contribution of Fe is its role as a mechanically stronger constituent within the Al matrix, which is reflected in the progressive increase in global microhardness (Fig. 10) and in the strength increase observed in both uniaxial tensile testing (Table 4) and PIP analysis (Table 5). In addition to this direct reinforcement effect, the presence of hard Fe particles within the deposit is also likely to influence the local deformation behavior of subsequently impinging particles during deposition. In particular, the increasing flattening ratio of Al splats with increasing Fe content (Table 3), together with the reduction in porosity and the gradual rise in Al splat hardness, is consistent with a progressive intensification of local deformation in the Al phase as Fe is incorporated. The peening effect of rebounding particles, particularly hard Fe particles, also contributes to the observed increase in local deformation and splat hardness. The rise in hardness measured in regions close to Al–Fe boundaries is also compatible with increasing local

Table 5
Mechanical properties of deposits derived from PIP test.

Composition	Cold-rolled Al (5 N) (strain of ~ 1.2) [75]	Al	Al–25Fe	Al–50Fe	Al–75Fe	Fe_{900}	Cold-rolled Fe (strain of ~ 1) [76]
Yield strength [MPa]	47	46 ± 2	66 ± 6	87 ± 7	117 ± 9	480 ± 25	460 ± 22
Tensile strength [MPa]	96	96 ± 2	129 ± 3	151 ± 7	207 ± 40	548 ± 29	546 ± 24

mechanical constraint and deformation heterogeneity. Overall, the combined microstructural and local mechanical data suggest that Fe incorporation promotes a denser and more mechanically constrained deposit architecture, particularly at low-to-intermediate retained Fe contents.

The variation of the key tensile properties as a function of the retained Fe content is summarized in Fig. 14, which provides a clear view of the composition–property relationships. The red lines in the plots correspond to sigmoidal curve fits. The tensile modulus of the Al deposit remained well below the values expected for bulk Al processed by conventional routes [77]. Previous studies have shown that elastic modulus in cold sprayed materials is strongly influenced by inter-splat boundary cracking and interfacial compliance, which reduce the efficiency of load transfer across the deposit architecture and can lower the modulus by 40–80% relative to the corresponding bulk material [78–82]. In this context, the substantially reduced modulus of the Al deposit is attributed primarily to incomplete inter-splat bonding and the presence of interfacial defects. Although residual porosity may contribute to the reduction in stiffness, its influence is likely secondary in the present deposits because the measured porosity levels are relatively low. By contrast, the Fe_{900} reference exhibited an effective tensile modulus much closer to that of bulk Fe [83]. While this behavior is consistent with the more favorable deposition conditions required to achieve sufficient build-up in pure Fe, it should be noted that the higher process temperature may also influence microstructural characteristics such as inter-splat bonding quality, residual stress state, and defect population. The interpretation of the composition-dependent trends presented herein is therefore focused primarily on the Al-containing deposits, which were all produced under identical processing conditions. As the retained Fe content increased in the Al–Fe deposits, the effective E, YS, and UTS all increased, but the strengthening trend progressively approached saturation beyond approximately 23–28 vol% retained Fe.

To interpret the E of the mixed deposits, both ROM and Hashin–Shtrikman (HS) bounds were considered, as shown in Fig. 14a. The calculations were performed following the methodologies reported in the literature for the ROM [70] and HS [84] models and were based on the retained phase fractions obtained from image analysis and the elastic moduli of the constituent phases. The experimentally measured modulus of the cold sprayed Al deposit (32.1 GPa) was used to represent the continuous matrix phase, thereby accounting for the influence of the cold sprayed microstructure on the matrix response. For the Fe phase, the experimentally measured modulus of the Fe_{900} deposit (184.2 GPa) was adopted instead of the bulk Fe modulus, as it provides a more representative of the cold sprayed condition. The ROM model provides idealized upper and lower limits based on iso-strain and iso-stress assumptions, respectively, whereas the HS model provides rigorous theoretical upper and lower bounds for the elastic response of a two-phase composite. Unlike the ROM approach, which assumes uniform stress or strain throughout the material, the HS model accounts for

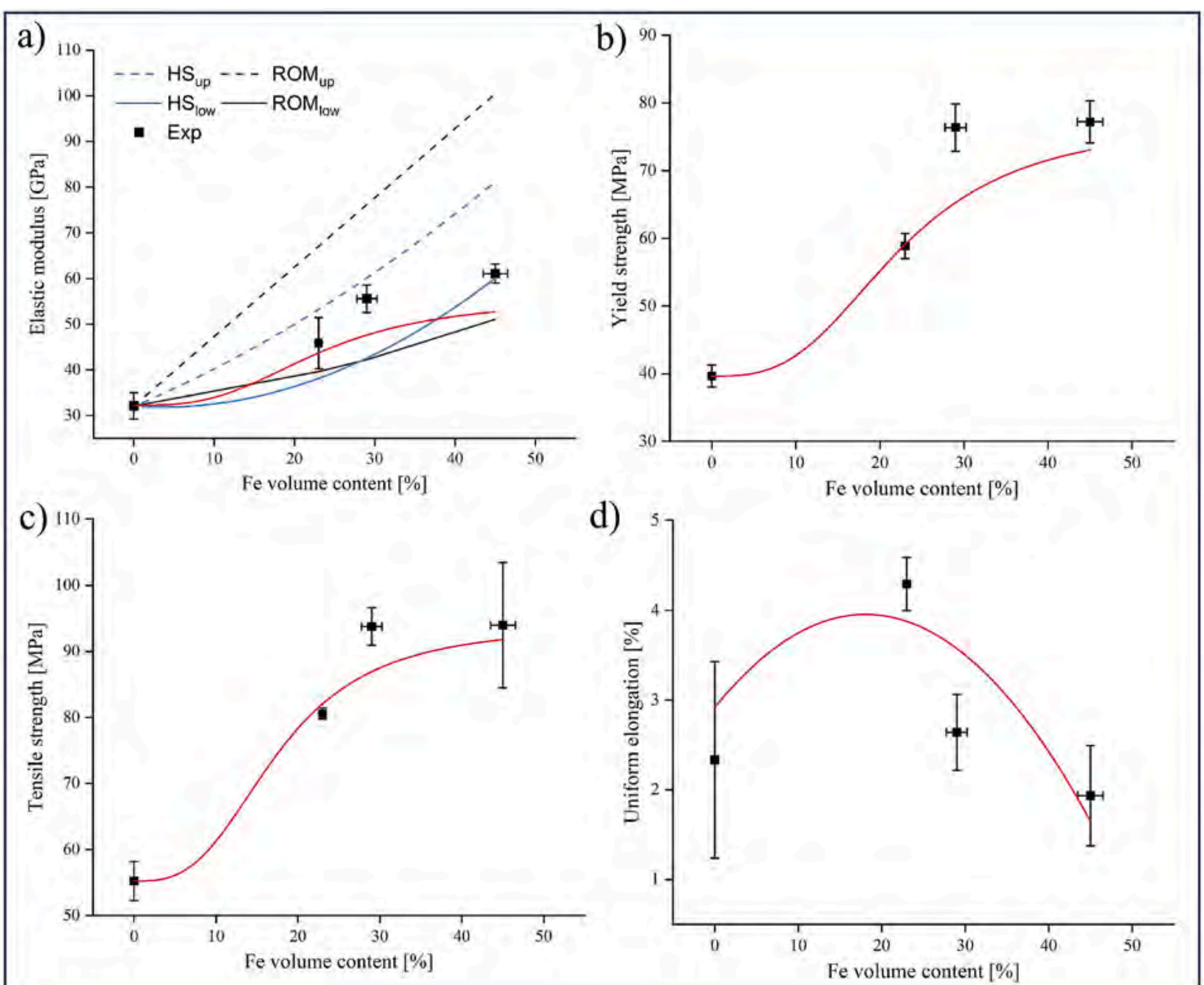

Fig. 14. Variation in a) effective elastic modulus, b) yield strength, c) tensile strength, and d) uniform elongation as a function of retained Fe content in the bimetallic deposits, as obtained from uniaxial tensile tests.

elastic interactions between the constituent phases through their elastic properties and volume fractions, resulting in more physically realistic bounds for the effective modulus of heterogeneous composites.

As expected, the measured modulus increased with increasing retained Fe content due to the higher stiffness of the Fe phase compared with Al. The experimental values are located between the ROM upper and lower bounds over the entire composition range. However, the iso-strain ROM prediction substantially overestimates the measured modulus, particularly at higher Fe contents, while the iso-stress prediction underestimates the reinforcing contribution of Fe. This indicates that the deposits exhibit partial load sharing between the Al-rich matrix and the Fe-rich phase, but remain far from the behavior of an ideal fully bonded composite.

Compared with the ROM predictions, the HS bounds provide a narrower and more realistic range for the effective modulus. The experimental values fall within or very close to the lower HS bound throughout the investigated composition range. This behavior suggests that the deposits mechanically behave as an Al-matrix composite reinforced by discrete Fe particles rather than as a continuous interconnected Fe-bearing structure. The proximity of the experimental values to the lower HS bound further indicates that the reinforcing efficiency of the Fe phase is limited by microstructural features inherent to the CS process, including imperfect inter-particle bonding, and heterogeneous phase distribution. Consequently, the measured modulus reflects not only the intrinsic stiffness of the constituent phases but also the effectiveness of load transfer through the deposited microstructure.

The indentation modulus values help to clarify this distinction further. For the Al deposit, the local indentation modulus measured within individual splats remained close to the bulk stiffness of Al, whereas the macroscopic tensile modulus was substantially lower. This difference highlights the contrast between the local elastic response of the splat material and the global stiffness of the deposited architecture. For Fe_{900}, the indentation modulus was even higher than the bulk-like tensile modulus, which may reflect a combination of crystallographic anisotropy and local residual stress effects at the splat scale. Accordingly, the local indentation response should be interpreted as a measure of splat-scale stiffness rather than a direct predictor of bulk tensile modulus.

The ductility of the deposits exhibited a non-monotonic dependence on retained Fe content (Fig. 14d), with the highest elongation observed for Al–25Fe. This indicates that a moderate amount of Fe provides the most favorable balance between strengthening and tensile deformability. In this regime, the Al matrix remains continuous, Fe particles are relatively well dispersed, and crack propagation is locally disrupted rather than proceeding along a single weak inter-splat path. The lower porosity of the mixed deposits relative to pure Al also suggests that the density of critical defects and unbonded regions is reduced, which likely contributes to the improved tensile response at the intermediate composition. At higher retained Fe contents, however, ductility decreased again, despite the continued increase in stiffness and strength. This reduction is consistent with the microstructural evolution observed in Section 3.1 and the fracture features discussed in Section 3.4. As the retained Fe content increases, Fe-rich regions become more clustered, the continuity of the Al matrix is reduced, and the density of Al–Fe interfaces increases. In addition, the progressive increase in both local and global hardness (Fig. 9a, Fig. 10) with increasing Fe content indicates a more mechanically constrained and strain-hardened deposit architecture, which further reduces the capacity for plastic deformation under tensile loading. Under these conditions, local stress concentrations and interfacial decohesion become more prominent, which promotes earlier crack initiation and more brittle crack propagation. Thus, while Fe addition enhances stiffness and strength, the associated changes in phase distribution and interface density eventually limit further gain in tensile performance.

4.3. Comparison of uniaxial tensile and PIP responses

Comparison between uniaxial tensile and PIP results provides additional insight into how the Al–Fe deposits respond under different loading conditions, as reflected in Fig. 15. In both methods, increasing the retained Fe content leads to higher strength, indicating that the overall strengthening trend is robust and not specific to a single test configuration. However, the absolute YS and UTS values obtained by PIP are consistently higher than those measured in uniaxial tension, with the difference becoming more pronounced at higher Fe contents.

These differences between PIP and tensile responses are consistent with the fundamentally different stress states involved in the two tests. Under uniaxial tension, the deposits are highly sensitive to early crack initiation and propagation at weakly bonded splat interfaces, which limits the measured ductility and reduces the attainable flow stress. Under PIP loading, such tensile crack-opening mechanisms are suppressed, allowing the material to sustain substantially larger plastic deformation before instability. Therefore, the higher strength and strain capacity indicated by the PIP results should not be interpreted as directly equivalent to tensile ductility, but rather as evidence that the deposits possess a greater capacity for plastic flow under constrained loading than is apparent from tensile tests alone.

This interpretation is consistent with previous studies on cold-sprayed and heterogeneous metallic materials [85–88], where compressive loading produced higher apparent strength and strain

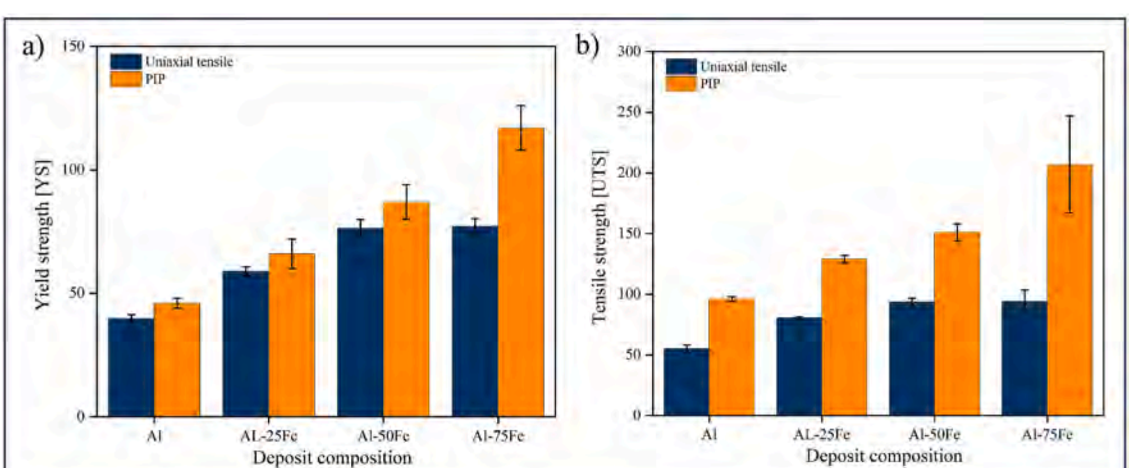

Fig. 15. Comparison between a) YS and b) UTS obtained by uniaxial tensile and PIP tests.

capacity than uniaxial tension. For example, cold-sprayed bulk Ti exhibited a compressive strength of 850 MPa compared with a tensile strength of only 180 MPa, while PIP studies on cold-sprayed Scalmalloy and friction-stir-welded AA5083 also reported higher indentation-derived elongation than tensile elongation. These differences were attributed to pores, particle/splat interfaces, and microstructural heterogeneity, which promote premature crack initiation and propagation in tension but have a smaller effect under compressive or constrained indentation loading.

The difference between the two test methods is particularly informative for the mixed deposits. For Al, Al–25Fe, and Al–50Fe, both methods show a similar qualitative evolution of strength with composition, even though the attainable strain capacity differs markedly. For Al–75Fe, the larger separation between tensile and PIP responses suggests that this composition remains especially sensitive to interface-controlled failure under tension, despite its relatively high resistance to plastic flow under constrained loading. These results highlight that, at high retained Fe contents, further improvement in tensile performance depends less on increasing reinforcement and more on improving inter-splat bonding and interfacial integrity.

Overall, the comparison between tensile and PIP behavior reinforces the conclusion that the mechanical response of the present Al–Fe deposits is governed by an interplay between phase composition, spatial distribution, and stress-state-dependent damage development. In this respect, the tensile response reflects the practical limitation imposed by the as-sprayed interfacial condition, whereas the PIP response provides a complementary indication of the plastic-flow capacity that can be sustained when tensile crack-opening mechanisms are suppressed. However, because PIP samples an effective indented volume that may contain different local fractions of Al matrix, Fe splats, pores, splat boundaries, and Fe-rich clusters, the extracted response should not be considered directly equivalent to the macroscopic fracture limited tensile response.

5. Conclusions

This study established a composition–structure–property relationship for Al–Fe bimetallic composites produced by cold spray additive manufacturing using online powder mixing of as-received powders. By systematically varying composition, the results showed how nominal feedstock composition is translated into retained phase fraction in the deposit and how this retained composition governs the resulting microstructure and mechanical performance. The main conclusions are as follows:

- Feedstock composition strongly influenced retained phase fraction and spatial distribution. Al consistently formed a continuous matrix, whereas retained Fe increasingly deviated from the nominal feedstock composition at higher Fe contents. Near-nominal retention was achieved only at low Fe fraction (Al–25Fe), while higher Fe contents led to progressively lower retained Fe and more evident clustering.
- Fe addition substantially modified the deposit microstructure. Relative to pure Al, the mixed deposits exhibited much lower porosity, decreasing to below 0.25%, together with a progressive increase in Al splat flattening ratio. These trends indicate that Fe incorporation promotes a denser deposit architecture and enhances deformation of the Al-rich matrix during deposition.
- Local mechanical measurements showed increasing heterogeneity with Fe addition. Al splats hardened progressively with increasing Fe content, Fe splats remained substantially harder than Al throughout the mixed deposits, and the indentation response near Al–Fe boundaries became increasingly constrained. These observations are consistent with a progressively more heterogeneous and mechanically constrained microstructure as retained Fe content increases.
- Bulk mechanical properties depended strongly on the retained Fe content and exhibited non-linear behavior. The effective tensile modulus, yield strength, and tensile strength all increased with Fe addition, but the strengthening trend approached saturation beyond approximately 23–28 vol% retained Fe. In contrast, ductility showed a non-monotonic trend, reaching a maximum at Al–25Fe, where the Al matrix remained continuous and Fe was relatively well dispersed. At higher Fe contents, ductility decreased as clustering, increasing interface density, and more brittle fracture modes became more prominent.
- Comparison between uniaxial tensile and PIP responses showed that both methods captured the same overall strengthening trend with increasing retained Fe content, but PIP indicated substantially greater strain capacity than tensile testing. This difference highlights the strong influence of stress state and interfacial damage on the measured mechanical response, and indicates that the present deposits can sustain greater plastic flow under constrained loading than is apparent from tensile tests alone.

Overall, the results show that the mechanical behavior of online-mixed Al–Fe cold sprayed deposits is governed not simply by nominal powder blending, but by the interplay between retained composition, its spatial distribution, and interface-controlled damage development. An intermediate retained Fe content provides the most favorable balance between stiffness, strength, and tensile deformability, offering useful guidance for the design of multi-material cold sprayed structural deposits. Future work will focus on investigating the influence of retained composition and microstructural architecture on the thermal, electrical, and corrosion properties of these bimetallic composites to further assess their application potential.

CRediT authorship contribution statement

Kiran Tulasagiri Raddi: Writing – original draft, Visualization, Validation, Methodology, Investigation, Formal analysis, Data curation. **Asghar Heydari Astaraee:** Writing – review & editing, Supervision, Methodology, Investigation, Formal analysis, Conceptualization. **Sara Bagherifard:** Writing – review & editing, Supervision, Resources, Project administration, Methodology, Funding acquisition, Conceptualization.

Declaration of competing interest

The authors declare that they have no known competing financial interests or personal relationships that could have appeared to influence the work reported in this paper.

Acknowledgments

This research received funding from the European Research Council (ERC) under the European Union's Horizon 2021 research and innovation programme (ArcHIDep ERC-Co project, grant agreement n. 101044228). Views and opinions expressed are, however, those of the authors only and do not necessarily reflect those of the European Union or the European Research Council Executive Agency. Neither the European Union nor the granting authority can be held responsible for them.

The authors are grateful to Plastometrex company (UK) for making their PLX-Benchtop available and for supporting the execution of the profilometry-based indentation plastometry tests.

Use of AI-based language editing tools

Portions of this manuscript were refined for grammar and clarity using an AI-based language editing tool (ChatGPT). The tool was used solely for linguistic editing and did not generate scientific content, analysis, or conclusions. All scientific content has been written, reviewed, and verified by the authors.

Data availability

Data will be made available on request.

References

[1] T. DebRoy, H.L. Wei, J.S. Zuback, T. Mukherjee, J.W. Elmer, J.O. Milewski, A. M. Beese, A. Wilson-Heid, A. De, W. Zhang, Additive manufacturing of metallic components – process, structure and properties, Prog. Mater Sci. 92 (2018) 112–224, https://doi.org/10.1016/J.PMATSCI.2017.10.001.

[2] W.E. King, A.T. Anderson, R.M. Ferencz, N.E. Hodge, C. Kamath, S.A. Khairallah, A. M. Rubenchik, Laser powder bed fusion additive manufacturing of metals; physics, computational, and materials challenges, Appl. Phys. Rev. 2 (2015) 041304, https://doi.org/10.1063/1.4937809.

[3] A. Bandyopadhyay, Y. Zhang, B. Onuike, Additive manufacturing of bimetallic structures, Virtual Phys. Prototyp. 17 (2022) 256–294, https://doi.org/10.1080/17452759.2022.2040738.

[4] H.R. Kotadia, G. Gibbons, A. Das, P.D. Howes, A review of Laser Powder Bed Fusion Additive Manufacturing of aluminium alloys: Microstructure and properties, Addit. Manuf. 46 (2021) 102155, https://doi.org/10.1016/J.ADDMA.2021.102155.

[5] L. Yao, A. Ramesh, Z. Xiao, Y. Chen, Q. Zhuang, Multimetal Research in Powder Bed Fusion: A Review, Materials 2023, Vol. 16, Page 4287 16 (2023) 4287. doi: 10.3390/MA16124287.

[6] Y. Li, B. Yang, M. Song, R. Lai, B. Liu, Y. Liu, Z. Wang, Y. Li, Aluminum/steel dissimilar material with high interfacial strength manufactured by additive friction stir deposition, J. Manuf. Process. 133 (2025) 491–502, https://doi.org/10.1016/J.JMAPRO.2024.11.080.

[7] A. Kumar, L. Shi, X. Zhang, X. Liu, Z. Xia, S.L. Sing, C. Wu, A. De, Solid state friction-based additive manufacturing of heterogeneous metallic composites: recent progress and future prospects, J. Manuf. Process. 161 (2026) 309–335, https://doi.org/10.1016/J.JMAPRO.2026.01.096.

[8] Z. Zhang, L. Wan, Y. Xie, Q. Wen, S. Chen, Y. Huang, Steel grid-reinforced aluminum matrix composite prepared via wire-based friction stir additive manufacturing, Virtual Phys. Prototyp. 20 (2025), https://doi.org/10.1080/17452759.2025.2451114.

[9] M.M. Patel, V.J. Badheka, A review on friction stir welding (FSW) process for dissimilar aluminium to steel metal systems, Weld. Int. 38 (2024) 91–115, https://doi.org/10.1080/09507116.2023.2291064.

[10] M. Acarer, B. Demir, An investigation of mechanical and metallurgical properties of explosive welded aluminum–dual phase steel, Mater. Lett. 62 (2008) 4158–4160, https://doi.org/10.1016/J.MATLET.2008.05.060.

[11] W. Du, Y. Chen, J. Chen, H. Li, Y.S. Wang, Bond Enhancement Mechanism of Aluminum–Steel Composite Plates during Cold Roll Bonding, J. Mater. Eng. Perform. 2026 (2026) 1–13, https://doi.org/10.1007/S11665-026-13683-8.

[12] V. Champagne, D. Helfritch, The unique abilities of cold spray deposition, Int. Mater. Rev. 61 (2016) 437–455, https://doi.org/10.1080/09506608.2016.1194948.

[13] M.A. Adaan-Nyiak, A.A. Tiamiyu, Recent advances on bonding mechanism in cold spray process: a review of single-particle impact methods, J. Mater. Res. 38 (2023) 69–95, https://doi.org/10.1557/s43578-022-00764-2.

[14] S. Bagherifard, J. Kondas, S. Monti, J. Cizek, F. Perego, O. Kovarik, F. Lukac, F. Gaertner, M. Guagliano, Tailoring cold spray additive manufacturing of steel 316 L for static and cyclic load-bearing applications, Mater. Des. 203 (2021) 109575, https://doi.org/10.1016/J.MATDES.2021.109575.

[15] R. Falco, S. Bagherifard, Cold Spray Additive Manufacturing: A Review of Shape Control Challenges and Solutions, Journal of Thermal Spray Technology 2025 34:4 34 (2025) 1023–1041. https://doi.org/10.1007/S11666-025-01970-0.

[16] M. Kumaravel, Y. Eynolghozzat, J. Gussone, F. Yan, A. Ardeshiri Lordejani, J. Haubrich, G. Requena, I.S. Berglund, M. Guagliano, S. Bagherifard, Elucidating the challenges in the development and deployment of refractory complex concentrated alloys for additive manufacturing, Addit. Manuf. 89 (2024) 104286, https://doi.org/10.1016/J.ADDMA.2024.104286.

[17] A. Ardeshiri Lordejani, L. Romanenghi, A. Pollastri, M. Guagliano, S. Bagherifard, Deposit shape control for local repair and welding by cold spray, J. Manuf. Process. 112 (2024) 45–59, https://doi.org/10.1016/J.JMAPRO.2024.01.023.

[18] S. Bagherifard, G. Roscioli, M.V. Zuccoli, M. Hadi, G. D'Elia, A.G. Demir, B. Previtali, J. Kondás, M. Guagliano, Cold Spray Deposition of Freestanding Inconel Samples and Comparative Analysis with Selective Laser Melting, J. Therm. Spray Technol. 26 (2017) 1517–1526, https://doi.org/10.1007/s11666-017-0572-3.

[19] S. Bagherifard, S. Monti, M.V. Zuccoli, M. Riccio, J. Kondás, M. Guagliano, Cold spray deposition for additive manufacturing of freeform structural components compared to selective laser melting, Mater. Sci. Eng. A 721 (2018) 339–350, https://doi.org/10.1016/j.msea.2018.02.094.

[20] M. Ashokkumar, D. Thirumalaikumarasamy, T. Sonar, S. Deepak, P. Vignesh, M. Anbarasu, An overview of cold spray coating in additive manufacturing, component repairing and other engineering applications, J. Mech. Behav. Mater. 31 (2022) 514–534, https://doi.org/10.1515/JMBM-2022-0056.

[21] H. Assadi, H. Kreye, F. Gärtner, T. Klassen, Cold spraying – a materials perspective, Acta Mater. 116 (2016) 382–407, https://doi.org/10.1016/j.actamat.2016.06.034.

[22] A.P.M. de Araujo, F.B.D.M. Carmelo, E.M. Rocha, C.S. Kiminami, P. Gargarella, Effects of Process Parameters on Cold Spray Additive Manufacturing of Quasicrystalline Al93Fe3Cr2Ti2 Alloy, Powders 2 (2023) 525–539, https://doi.org/10.3390/powders2030033.

[23] P. Kindermann, M. Strasser, M. Wunderer, I. Uensal, M. Horn, C. Seidel, Cold spray forming: a novel approach in cold spray additive manufacturing of complex parts using 3D-printed polymer molds, Prog. Addit. Manuf. 9 (2024) 1567–1578, https://doi.org/10.1007/s40964-023-00521-9.

[24] P. Yu, Y. Xie, S. Yin, R. Lupoi, Fabrication of Ta-Ag composite deposits via cold spray: Investigation of bonding mechanism and deposition behavior, Journal of Advanced Joining Processes 6 (2022) 100127, https://doi.org/10.1016/j.jajp.2022.100127.

[25] A. Moridi, S.M. Hassani-Gangaraj, M. Guagliano, M. Dao, Cold spray coating: Review of material systems and future perspectives, Surf. Eng. 30 (2014) 369–395, https://doi.org/10.1179/1743294414Y.0000000270.

[26] M. Bashirzadeh, F. Azarmi, C.P. Leither, G. Karami, Investigation on relationship between mechanical properties and microstructural characteristics of metal matrix composites fabricated by cold spraying technique, Appl. Surf. Sci. 275 (2013) 208–216, https://doi.org/10.1016/J.APSUSC.2012.12.166.

[27] T. Liu, W.A. Story, L.N. Brewer, Effect of Heat Treatment on the Al-Cu Feedstock Powders for Cold Spray Deposition, Metall. Mater. Trans. A 50 (2019) 3373–3387, https://doi.org/10.1007/s11661-019-05230-z.

[28] S.M.M. Rizvi, M.J. Uddin, C. McRobie, J. Hartmann, A. Malakar, K. Yano, D. Barton, F.Y. Tsai, F. Laggner, B. Gwalani, E. Kautz, Ultrafine-Grained Al/Al2Cu Composite Formation via Friction Stir Processing of Cold-Sprayed Coatings, JOM 2025 (2025) 1–12, https://doi.org/10.1007/S11837-025-07741-0.

[29] H.T. Wang, C.J. Li, G.J. Yang, C.X. Li, Cold spraying of Fe/Al powder mixture: Coating characteristics and influence of heat treatment on the phase structure, Appl. Surf. Sci. 255 (2008) 2538–2544, https://doi.org/10.1016/J.APSUSC.2008.07.127.

[30] H.T. Wang, C.J. Li, G.C. Ji, G.J. Yang, Annealing effect on the intermetallic compound formation of cold sprayed Fe/Al, J. Therm. Spray Technol. 21 (2012) 571–577, https://doi.org/10.1007/S11666-011-9722-1.

[31] H. Wang, F. An, X. Bai, H. Yao, M. Zhang, Q. Chen, G. Ji, C.S. Ramachandran, Improvement of Microstructure and Sliding Wear Property of Cold-Sprayed FeAl Intermetallic Compound Coating by Annealing Treatment, Coatings 2023, Vol. 13, Page 1260 13 (2023) 1260. doi: 10.3390/COATINGS13071260.

[32] H.T. Wang, C.J. Li, G.J. Yang, C.X. Li, Q. Zhang, W.Y. Li, Microstructural characterization of cold-sprayed nanostructured FeAl intermetallic compound coating and its ball-milled feedstock powders, J. Therm. Spray Technol. 16 (2007) 669–676, https://doi.org/10.1007/S11666-007-9089-5/FIGURES/10.

[33] C.J. Li, H.T. Wang, G.J. Yang, C.G. Bao, Characterization of high-temperature abrasive wear of cold-sprayed FeAl intermetallic compound coating, J. Therm. Spray Technol. 20 (2011) 227–233, https://doi.org/10.1007/S11666-010-9545-5/FIGURES/6.

[34] G.J. Yang, H.T. Wang, C.J. Li, C.X. Li, Effect of annealing on the microstructure and erosion performance of cold-sprayed FeAl intermetallic coatings, Surf. Coat. Technol. 205 (2011) 5502–5509, https://doi.org/10.1016/J.SURFCOAT.2011.06.033.

[35] Y. Wang, N. Deng, Z. Tong, Z. Zhou, The effect of Fe/Al Ratio and Substrate Hardness on Microstructure and Deposition Behavior of Cold-Sprayed Fe/Al Coatings, Materials 16 (2023) 878, https://doi.org/10.3390/ma16020878.

[36] R. Qian, Q. Wang, W. Niu, Y. Shao, C. Wei, Influence of Aluminum content on the microstructure, corrosion property, and tribological performance of cold-sprayed Fe-Al coatings, Mater. Sci. Technol. (2025), https://doi.org/10.1177/02670836251412338.

[37] Y. Liu, Z. Jia, Y. Zhang, Effect of Al Content on the Microstructure and Corrosion Resistance of Low-Pressure Cold-Sprayed Fe-Al Coatings, Materials 2026, Vol. 19, 19 (2026) 1852. doi: 10.3390/MA19091852.

[38] L. Palenikova, V. Jan, J. Čupera, J. Cizek, Microstructure of Fe-Al binary cold spray thick deposit after annealing, METAL 2014 - 23rd International Conference on Metallurgy and Materials, Conference Proceedings (2014) 1328–1333.

[39] P. Richer, B. Jodoin, L. Ajdelsztajn, E.J. Lavernia, Substrate Roughness and Thickness Effects on Cold Spray Nanocrystalline Al-Mg Coatings, J. Therm. Spray Technol. 15 (2006) 246–254, https://doi.org/10.1361/105996306X108174.

[40] K. Spencer, M.X. Zhang, The use of kinetic metallization to form intermetallic reinforced composite coatings by post-spray heat treatment, Surf. Coat. Technol. 203 (2009) 3019–3025, https://doi.org/10.1016/J.SURFCOAT.2009.03.019.

[41] H.Y. Lee, S.H. Jung, S.Y. Lee, K.H. Ko, Alloying of cold-sprayed Al–Ni composite coatings by post-annealing, Appl. Surf. Sci. 253 (2007) 3496–3502, https://doi.org/10.1016/J.APSUSC.2006.07.053.

[42] A. Bacciochini, M.I. Radulescu, Y. Charron-Tousignant, J. Van Dyke, M. Nganbe, M. Yandouzi, J.J. Lee, B. Jodoin, Enhanced reactivity of mechanically-activated nano-scale gasless reactive materials consolidated by coldspray, Surf. Coat. Technol. 206 (2012) 4343–4348, https://doi.org/10.1016/j.surfcoat.2012.02.024.

[43] A.C. Liberati, H. Che, P. Vo, S. Yue, Observation of an indirect Deposition effect while Cold Spraying Sn-Al mixed Powders onto Carbon Fiber Reinforced Polymers, J. Therm. Spray Technol. 29 (2020) 134–146, https://doi.org/10.1007/S11666-019-00967-W/FIGURES/15.

[44] T. Novoselova, P. Fox, R. Morgan, W. O'Neill, Experimental study of titanium/aluminium deposits produced by cold gas dynamic spray, Surf. Coat. Technol. 200 (2006) 2775–2783, https://doi.org/10.1016/J.SURFCOAT.2004.10.133.

[45] L. Shen, L. yan Kong, T. ying Xiong, H. Du, T. fan Li, Preparation of TiAl3-Al composite coating by cold spraying, Transactions of Nonferrous Metals Society of China 19 (2009) 879–882. doi: 10.1016/S1003-6326(08)60369-6.

[46] H.Y. Lee, S.H. Jung, S.Y. Lee, K.H. Ko, Fabrication of cold sprayed Al-intermetallic compounds coatings by post annealing, Mater. Sci. Eng. A 433 (2006) 139–143, https://doi.org/10.1016/J.MSEA.2006.06.044.

[47] T. Novoselova, S. Celotto, R. Morgan, P. Fox, W. O`Neill, Formation of TiAl intermetallics by heat treatment of cold-sprayed precursor deposits, J. Alloys Compd. 436 (2007) 69–77, https://doi.org/10.1016/J.JALLCOM.2006.06.101.
[48] X.L. Zhou, S.J. Mou, X.K. Wu, J.S. Zhang, Deposition behavior of mixed binary metallic powders in cold spraying process, Appl. Surf. Sci. 257 (2011) 10628–10633, https://doi.org/10.1016/J.APSUSC.2011.07.061.
[49] Z. Zhao, J. Tang, N.U.H. Tariq, J. Wang, X. Cui, T. Xiong, Microstructure and Corrosion Behavior of Cold-Sprayed Zn-Al Composite Coating, Coatings 2020, Vol. 10, Page 931 10 (2020) 931. doi: 10.3390/COATINGS10100931.
[50] J. Martin, A. Maizeray, C. Da Silva Tousch, G. Marcos, T. Czerwiec, G. Henrion, A new strategy to prepare alumina-zirconia composite or multilayered coatings by combining cold-spray deposition and plasma electrolytic oxidation, Mater. Today Commun. 36 (2023) 106676, https://doi.org/10.1016/J.MTCOMM.2023.106676.
[51] O. Furukimi, H. Katafuchi, M. Aramaki, M. Kozin, S. Oue, K. Yoshida, I. Narita, N. Yamada, M. Yamamoto, Wear Resistance of Industrial Pure Iron Treated by Nitriding and Quenching Followed by Aging Process, Mater. Trans. 57 (2016) 1587–1592, https://doi.org/10.2320/matertrans.H-M2016825.
[52] E. Lucon, K. Abiko, M. Lambrecht, B. Rehmer, Tensile Properties of Commercially Pure, High Purity and Ultra High Purity Iron: results of an International Round-Robin, Gaithersburg, MD (2015), https://doi.org/10.6028/NIST.TN.1879.
[53] J. Chen, Research on Aluminum Alloy Materials and Application Technology for Automotive Lightweighting, Academic Journal of Materials & Chemistry 4 (2023), https://doi.org/10.25236/AJMC.2023.040601.
[54] S. Li, X. Yue, Q. Li, H. Peng, B. Dong, T. Liu, H. Yang, J. Fan, S. Shu, F. Qiu, Q. Jiang, Development and applications of aluminum alloys for aerospace industry, J. Mater. Res. Technol. 27 (2023) 944–983, https://doi.org/10.1016/j.jmrt.2023.09.274.
[55] A.A. Tiamiyu, C.A. Schuh, Particle flattening during cold spray: Mechanistic regimes revealed by single particle impact tests, Surf. Coat. Technol. 403 (2020) 126386, https://doi.org/10.1016/J.SURFCOAT.2020.126386.
[56] W.C. Oliver, G.M. Pharr, An improved technique for determining hardness and elastic modulus using load and displacement sensing indentation experiments, J. Mater. Res. 7 (1992) 1564–1583, https://doi.org/10.1557/JMR.1992.1564.
[57] ISO 6892-1:2019 - Metallic materials — Tensile testing — Part 1: Method of test at room temperature, (n.d.). https://www.iso.org/standard/78322.html (accessed May 12, 2026).
[58] ASTM E3499 Standard Test Method for Indentation Plastometry of Metallic Materials, (2025). https://doi.org/10.1520/E3499-25.
[59] B.C. Sousa, D.L. Cote, M.A. Priddy, V.K. Champagne, Profilometry-based Indentation Plastometry Brings speed and Accuracy to Metallurgical R&D, Adv. Mater. Process. 180 (2022) 19–24, https://doi.org/10.31399/ASM.AMP.2022-03.P019.
[60] Y.T. Tang, J.E. Campbell, M. Burley, J. Dean, R.C. Reed, T.W. Clyne, Profilometry-based indentation plastometry to obtain stress-strain curves from anisotropic superalloy components made by additive manufacturing, Materialia (oxf). 15 (2021) 101017, https://doi.org/10.1016/J.MTLA.2021.101017.
[61] T.W. Clyne, J.E. Campbell, M. Burley, J. Dean, Profilometry-Based Inverse Finite Element Method Indentation Plastometry, (2021). doi: 10.1002/adem.202100437.
[62] S. Yin, X. Wang, X. Suo, H. Liao, Z. Guo, W. Li, C. Coddet, Deposition behavior of thermally softened copper particles in cold spraying, Acta Mater. 61 (2013) 5105–5118, https://doi.org/10.1016/j.actamat.2013.04.041.
[63] C. Huang, A. List, J. Shen, B. Fu, S. Yin, T. Chen, B. Klusemann, F. Gärtner, T. Klassen, Tailoring powder strengths for enhanced quality of cold sprayed Al6061 deposits, Mater. Des. 215 (2022) 110494, https://doi.org/10.1016/j.matdes.2022.110494.
[64] F.Z. Li, Z.J. Liu, Q. Jin, Z.M. Yu, E. Liu, Investigation on work softening behavior of aluminum and its alloys with iron, J. Mater. Eng. Perform. 6 (1997) 172–176, https://doi.org/10.1007/S11665-997-0010-7/METRICS.
[65] S. Yamamoto, M. Mizuno, A. Kirihata, Age softening of worked Al-Fe alloys, Japan Institute of Metals 56 (1992) 142–147, https://doi.org/10.2320/JINSTMET1952.56.2_142.
[66] P. Filippov, U. Koch, Nanoindentation of Aluminum Single Crystals: Experimental Study on Influencing Factors, Materials 2019, Vol. 12, Page 3688 12 (2019) 3688. doi: 10.3390/MA12223688.
[67] S. Takaki, T. MasuMura, T. TsuchiyaMa, Young's modulus of single crystalline iron and elastic stiffness, Tetsu-to-Hagane/journal of the Iron and Steel Institute of Japan 106 (2020) 679–682, https://doi.org/10.2355/TETSUTOHAGANE.TETSU-2019-129.
[68] G.M. Pharr, T.Y. Tsui, A. Bolshakov, W.C. Oliver, Effects of residual stress on the measurement of hardness and elastic modulus using nanoindentation, Materials Research Society Symposium - Proceedings 338 (1994) 127–134, https://doi.org/10.1557/PROC-338-127/METRICS.
[69] J.E. Rivera-Salinas, K.M. Gregorio-Jáuregui, J.A. Romero-Serrano, A. Cruz-Ramírez, E. Hernández-Hernández, A. Miranda-Pérez, V.H. Gutierréz-Pérez, Simulation on the Effect of Porosity in the Elastic Modulus of SiC Particle Reinforced Al Matrix Composites, Metals 2020, Vol. 10, Page 391 10 (2020) 391. doi: 10.3390/MET10030391.
[70] H.S. Kim, On the rule of mixtures for the hardness of particle reinforced composites, Mater. Sci. Eng. A 289 (2000) 30–33, https://doi.org/10.1016/S0921-5093(00)00909-6.
[71] A.C. Hall, D.J. Cook, R.A. Neiser, T.J. Roemer, D.A. Hirschfeld, The effect of a simple annealing heat treatment on the mechanical properties of cold-sprayed aluminum, Journal of Thermal Spray Technology 2006 15:2 15 (2006) 233–238. https://doi.org/10.1361/105996306X108138.
[72] R. Huang, M. Sone, W. Ma, H. Fukanuma, The effects of heat treatment on the mechanical properties of cold-sprayed coatings, Surf. Coat. Technol. 261 (2015) 278–288, https://doi.org/10.1016/J.SURFCOAT.2014.11.017.
[73] G. Vinay, S. Halder, R. Kant, H. Singh, Examining the contribution of tamping effect on inter-splat bonding during cold spray, Mater. Sci. Eng. A 893 (2024) 146112, https://doi.org/10.1016/J.MSEA.2024.146112.
[74] Y. Wang, B.C. Wong, T.M. Chan, R. Voyle, Towards Strength–Ductility Synergy in Cold Spray for Manufacturing and Repair Application: A Review, Processes 2024, Vol. 12, Page 2216 12 (2024) 2216. doi: 10.3390/PR12102216.
[75] Y.-Y. Lv, L.-F. Zhang, G.-X. Wang, Y. Xiong, Effect of Rolling and Annealing on Microstructure and Mechanical Properties of High Purity Aluminum, (2017) 93–98. doi: 10.2991/AME-17.2017.17.
[76] H. Feng, L. Wang, S. Cui, N. Hansen, F. Fang, X. Zhang, Microstructure and strengthening mechanisms of nanolamellar structures in ultrastrong drawn iron wires, Scr. Mater. 200 (2021) 113906, https://doi.org/10.1016/J.SCRIPTAMAT.2021.113906.
[77] J. Ha, J. Fones, B.L. Kinsey, Y.P. Korkolis, Plasticity and Formability of Annealed, Commercially-Pure Aluminum: Experiments and Modeling, Materials 2020, Vol. 13, Page 4285 13 (2020) 4285. doi: 10.3390/MA13194285.
[78] V. Luzin, K. Spencer, M.X. Zhang, Residual stress and thermo-mechanical properties of cold spray metal coatings, Acta Mater. 59 (2011) 1259–1270, https://doi.org/10.1016/J.ACTAMAT.2010.10.058.
[79] S. Sampath, X.Y. Jiang, J. Matejicek, L. Prchlik, A. Kulkarni, A. Vaidya, Role of thermal spray processing method on the microstructure, residual stress and properties of coatings: an integrated study for Ni–5 wt.%Al bond coats, Materials Science and Engineering: A 364 (2004) 216–231, https://doi.org/10.1016/J.MSEA.2003.08.023.
[80] N.M. Chavan, M. Ramakrishna, P.S. Phani, D.S. Rao, G. Sundararajan, The influence of process parameters and heat treatment on the properties of cold sprayed silver coatings, Surf. Coat. Technol. 205 (2011) 4798–4807, https://doi.org/10.1016/J.SURFCOAT.2011.04.063.
[81] G. Sundararajan, N.M. Chavan, G. Sivakumar, P. Sudharshan Phani, Evaluation of parameters for assessment of inter-splat bond strength in cold-sprayed coatings, J. Therm. Spray Technol. 19 (2010) 1255–1266, https://doi.org/10.1007/S11666-010-9527-7.
[82] G. Sundararajan, N.M. Chavan, S. Kumar, The elastic modulus of cold spray coatings: Influence of inter-splat boundary cracking, J. Therm. Spray Technol. 22 (2013) 1348–1357, https://doi.org/10.1007/S11666-013-0034-5.
[83] J.A. Benito, J.M. Manero, J. Jorba, A. Roca, Change of Young's modulus of cold-deformed pure iron in a tensile test, Metallurgical and Materials Transactions A 2005 36:12 36 (2005) 3317–3324. doi: 10.1007/S11661-005-0006-6.
[84] Z. Hashin, S. Shtrikman, A variational approach to the theory of the elastic behaviour of multiphase materials, J. Mech. Phys. Solids 11 (1963) 127–140, https://doi.org/10.1016/0022-5096(63)90060-7.
[85] O. Kovarik, J. Cizek, S. Yin, R. Lupoi, M. Janovska, J. Cech, J. Capek, J. Siegl, T. Chraska, Mechanical and Fatigue Properties of Diamond-Reinforced Cu and Al Metal Matrix Composites Prepared by Cold Spray, Journal of Thermal Spray Technology 2022 31:1 31 (2022) 217–233. doi: 10.1007/S11666-022-01321-3.
[86] Z. Li, X. Yang, J. Zhang, B. Zheng, Y. Zhou, A. Shan, E.J. Lavernia, Microstructure Evolution and Mechanical Behavior of Cold-Sprayed, Bulk Nanostructured Titanium, Metallurgical and Materials Transactions A 2014 45:11 45 (2014) 5017–5028. doi: 10.1007/S11661-014-2434-7.
[87] A. Lama, R. Sarvesha, D. Garcia, T. Dolmetsch, T. Wang, R. Eberheim, K. Ross, A. Agarwal, Macroscale property assessment and indentation characteristics of thick section friction stir welded AA 5083, Mater. Sci. Eng. A 880 (2023) 145306, https://doi.org/10.1016/J.MSEA.2023.145306.
[88] A. Lama, R. Sarvesha, D. John, T. Paul, A. Sukumaran, A. Agarwal, Role of nitrogen and helium gases on microstructure and anisotropic mechanical properties of cold-sprayed scalmalloy deposits, J. Mater. Res. Technol. 30 (2024) 1341–1353, https://doi.org/10.1016/J.JMRT.2024.03.201.